The articles published in the Journal of Casting & Materials Engineering have been given a favorable opinion by the rewievers designated by the Editorial Board.

www:
https://journals.agh.edu.pl/jcme/

AGH UNIVERSITY OF SCIENCE AND TECHNOLOGY PRESS KRAKOW 2022

Wydawnictwa AGH (AGH University of Science and Technology Press)
al. A. Mickiewicza 30, 30-059 Kraków
tel. 12 617 32 28, 12 638 40 38
e-mail: redakcja@wydawnictwoagh.pl
http://www.wydawnictwa.agh.edu.pl

Contents

Journal of Casting & Materials Engineering Vol. 6 No. 1 (2022) 1–7
https://doi.org/10.7494/jcme.2022.6.1.1

The Correlation between Solidification Rates, Microstructure Integrity and Tensile Plastic Behaviour in 4.2 wt.% Silicon Strengthened Ductile Iron

Giuliano Angella[a*], Marcello Taloni[a], Riccardo Donnini[a], Franco Zanardi[b]

[a] Research Institute CNR-ICMATE, Department of Chemical Sciences and Materials Technology, via R. Cozzi 53, 20125 Milano (MI), Italy
[b] Zanardi Fonderie S.p.A., via Nazionale 3, 37046 Minerbe (VR), Italy
e-mail: giuliano.angella@cnr.it

Received: 26 October 2021/Accepted: 14 December 2021/Published online: 14 January 2022.
This article is published with open access at AGH University of Science and Technology Journals.

Paper presented at the EUROMAT 2021: Cast Irons and Steel Making. September 13–17, 2021, Virtual Conference.

Abstract

High Silicon Strengthened Ductile Iron (HSiSDI) with 4.2 wt.% of silicon was produced in Y-blocks with different thicknesses to investigate the effects of the solidification rate on microstructure integrity and tensile mechanical properties. With decreasing solidification rates, the graphite degeneracy with the appearance of chunky graphite became more significant at the highest silicon contents, so chemical ordering and graphite degeneracy seemed to be qualitative explanations of tensile property degradation. However, a deeper analysis of the relationship between solidification rate, microstructure and tensile properties was realized through an innovative approach based on the Matrix Assessment Diagram (MAD), where the parameters of Voce equation resulting from best-fitting the experimental tensile flow curves of a significant number of HSiSDI samples, were plotted. For 3.5 wt.% silicon content, the MAD analysis indicated that the microstructure was sound for any solidification rate, while for 4.5 wt.% the microstructure was sound only for the fastest solidification rates. For 4.2 wt.% silicon content the MAD analysis pointed out that the tensile plastic behaviour and the microstructure integrity was in between the 3.5 and 4.5 wt.% silicon contents, representing a composition threshold where the reliable microstructures were only found with the fastest solidification rates, while considerable variability was found for the slowest ones. Support to the MAD analysis results was given from microstructure observations.

Keywords:

strain hardening; constitutive equations; integrity assessment; ductile irons; high silicon content

1. INTRODUCTION

High Silicon Strengthened Ductile Irons (HSiSDIs) with alloying Si contents in the range 3.2–4.3 wt.% have recently been considered in the European Standard EN 1563:2018. They are fully ferritic because of the Si solid solution causing an increase of yield and tensile strengths with a moderate reduction of ductility [1–4], and a better machinability than ferritic and ferritic-pearlitic ductile irons with similar strengths [1, 2, 5–8]. However, besides the good balance of tensile properties, HSiSDIs impact resistance decreases significantly with increasing silicon alloying [9–12]. Indeed, tensile strength is maximum at 4.2–4.3 wt.% of Si content [4, 13, 14], and above this critical content both yield and tensile strength decrease rapidly, while ductility decreases rapidly above 3.5 wt.%, achieving zero ductility at about 5.0 wt.%, which has been attributed to progressive chemical ordering of the ferritic matrix with increasing silicon content. However, chunky graphite might also have a detrimental contribution to ductily as recently reported in [15]. Indeed, Si also promotes graphite degeneracy, resulting in a decrease in nodularity, and also the chunky graphite formation [4, 16–18]. Chunky graphite is commonly found in conventional ductile irons produced in heavy sections with slow solidification rates [18–22], where it has been reported a significant decrease of ductility and ultimate tensile strength [20, 21], although the most detrimental effect of chunky graphite is on the fatigue resistance [23, 24]. Futhermore other microstructure parameters like nodule count, size and roundness of the graphite nodules can affect the mechanical properties [3, 25–29].

Low structural integrity, i.e. metallurgical discontinuities and defects such as degenerated graphite, shrinkages, inclusions, etc., may have adverse effects on the final mechanical properties of ductile irons.

According to the literature [30–34] tensile tests are the simplest and useful experimental examinations for assessing the integrity of ductile irons. A new experimental method, namely the Voce approach, based on the mathematical modelling

of the tensile flow curves by means of the dislocation-density-related Voce constitutive equation, seems to allow the classification of the process-microstructure relations and the integrity assessment of different ductile irons grades [35–37]. The Voce equation is defined as:

$$\sigma = \sigma_V + (\sigma_0 - \sigma_V) \cdot \exp\left(\frac{\varepsilon_p}{\varepsilon_c}\right) \quad (1)$$

where:

- σ – true flow stress;
- ε_p – true plastic strain;
- σ_V – saturation stress achieved asymptotically with plastic straining;
- σ_0 – back-extrapolated stress to $\varepsilon_p = 0$;
- ε_c – characteristic transient strain that defines the rate with which σ_V is achieved.

According to this approach, two diagrams are defined: the first one is the Matrix Assessment Diagram (MAD) graphically represented as $1/\varepsilon_c$ vs. Θ_o, the Voce parameters obtained by fitting the differential experimental flow curves with the differential form of Equation (1), that is:

$$\frac{d\sigma}{d\varepsilon_p} = \Theta_o - \frac{d\sigma}{d\varepsilon_c} \quad (2)$$

MAD allows the univocal identification of different ductile iron grades, i.e. produced through different production routes and having different chemical composition, such as Austempered Ductile irons (ADI) and Isothermal Ductile Irons (IDI) [35–37]. The second diagram is called Integrity Assessment Diagram (IAD) and is represented by plotting the experimental elongation at failure vs. the theoretical one determined according to the Voce formalism. IAD appears to be able to identify the potential presence of defects.

The present paper is focused on the study of the effects of various cooling times on the tensile mechanical properties and microstructural integrity of different High Silicon Strengthened Ductile Iron (HSiSDI) samples with 4.2 wt.% of Si and manufactured through Y-blocks with different thicknesses. According to Voce approach, tensile flow curves were modelled using the constitutive Voce equation, and Voce parameters are derived from the best fittings. Knowing these parameters, MAD and IAD are represented and microstructural results are correlated.

2. EXPERIMENTAL

HSiSDI with nominal 4.2 wt.% of Si, which chemical composition is reported in Table 1, was produced by gravity pouring the molten metal through the pouring basin to the pattern plate in order to obtain three Y-block of 25, 50 and 75 mm thicknesses and a Lynchburg sample with diameter Ø = 25 mm complying with ASTM A 536-84(2019)e1. Thus, the different samples were produced under the same conditions. Therefore, it is worth mentioning that because of the different geometry and wall thickness of the molds, the cooling rate, which was not experimentally measured, changed between the four classes of samples.

Table 1
Chemical composition [wt.%]

C	Si	Mg	Mn	P	S	Fe
3.55	4.20	0.048	0.12	0.037	0.006	Bal.

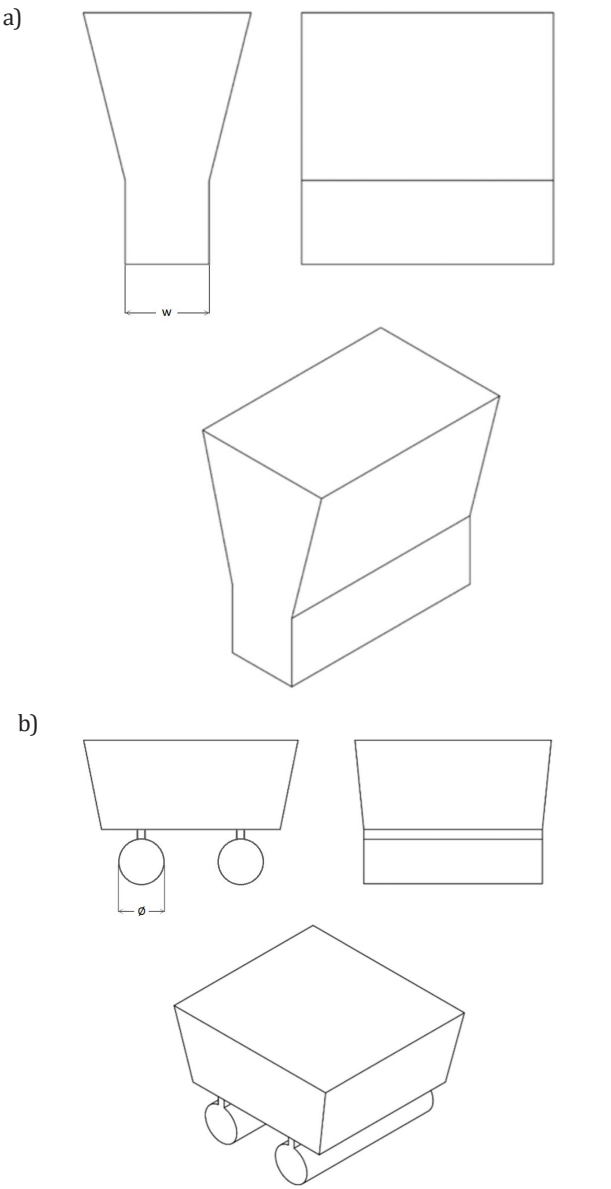

Fig. 1. Simplified representations of the molds used in the casting procedure: a) sketch of the three Y-molds, where the thickness w is equal to 25, 50, 75 mm respectively; b) sketch of the Lynchburg mold where the diameter Ø = 25 mm

A simplified representation of the Y-molds and Lynchburg mold is reported in Figure 1.

The microstructural characterization was performed using a Hitachi SU-70 high resolution scanning electron microscope. Through image analysis and complying with ASTM E2567-16a, nodule count, nodularity, mean diameter of graphite spheroids, area fractions of graphite and pearlite, and the presence of chunky graphite were found.

Tensile tests were carried out according to ASTM E8/E8M at strain rate 10^{-4} s^{-1} on round specimens with initial gauge diameter d_o = 12.5 mm and gauge length l_o = 50 mm.

3. RESULTS

3.1. Microstructure

Table 2 reports the mean values of the microstructural parameters resulting from the image analysis, while Figure 2a–d shows selected micrographs of the HSiSDIs analyzed.

Table 2
Microstructure analysis results of the investigated HSiSDI of 4.2 wt.% Si content produced through different molds

Mold	Nodularity [%]	Nodule Count [Nr/mm^2]	Nodule size [µm]	Chunky graphite
L25 mm	74.4 ±1.8	149.8 ±1.9	18.6 ±0.4	No
Y25 mm	85.4 ±1.1	210.6 ±2.0	20.0 ±0.3	No
Y50 mm	82.2 ±1.3	125.6 ±2.0	26.2 ±0.5	Traces
Y75 mm	83.3 ±1.0	107.3 ±1.9	28.5 ±0.6	Traces

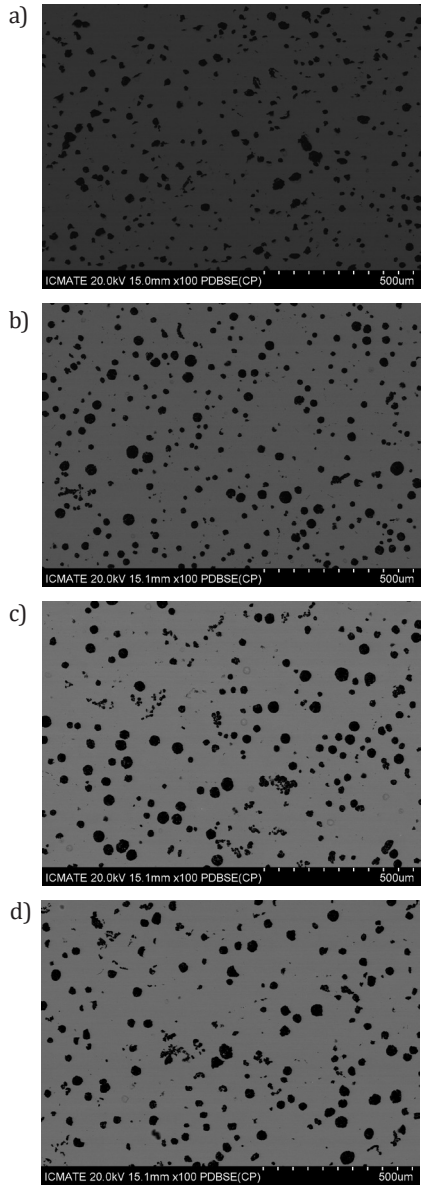

Fig. 2. Back Scattered Electron Imaging micrographs of HSiSDIs, with 4.2 wt.% of Si content, produced through: a) 25 mm Lynchburg; b) 25 mm Y-block; c) 50 mm Y-block; d) 75 mm Y-block molds

According to these data, the microstructure of the ductile irons produced through a Lynchburg mold of 25 mm (L25 mm) diameter shows the lowest nodularity and degenerated graphite aggregates. Samples Y25 mm shows greater nodularity, although graphite degeneration is also observable in this case. Increasing the thickness (samples Y50–Y75 mm) a reduction of the nodularity is observed. Furthermore, the appearance of chunky graphite is seen in Figure 2c, d.

3.2. Strain hardening analysis results, and MAD and IAD analysis

According to the Voce approach it was possible to define the strain hardening parameters $1/\varepsilon_c$ and Θ_o necessary to define the Matrix Assessment Diagram (MAD) reported in Figure 3 for Y50–Y75 mm samples. For comparison purposes, the graph also reports the data provided by a previous research [15] aimed to study the strain hardening behavior of HSiSDIs samples with various Si content, i.e. 3.5 wt.% and 4.5 wt.%, produced through Y50–Y75 mm molds [15].

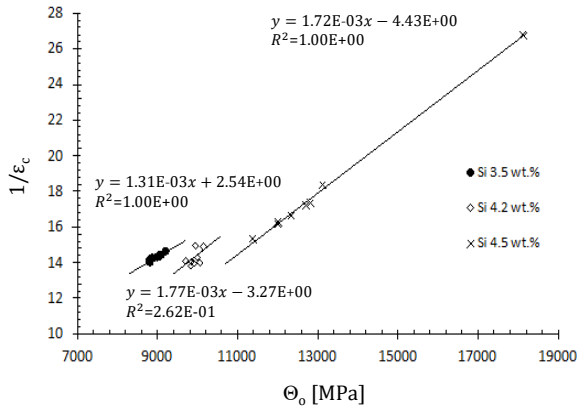

Fig. 3. Matrix Assessment Diagram (MAD) of Y50–Y75 mm HSiSDIs with Si content of 4.2 wt.%. For comparison, the data of a previous research [15] on HSiSDI samples with 3.5 wt.% and 4.5 wt.% are reported

The Voce parameters related to the three different kind of specimens, i.e 3.5, 4.2 and 4.5 wt.% Si content respectively, characterized by different chemical composition, lied in a specific region of MAD and on a specific line, namely $1/\varepsilon_c = m\Theta_o + C$. According to the Voce approach, σ_V defines the strenght of the material and it is related to Voce parameters through the expression:

$$\sigma_V = \varepsilon_c \cdot \Theta_o \tag{3}$$

so, σ_V can be rewritten as $\sigma_V = \Theta_o/(m\Theta_o + C)$. Consistently with the physical meaning of the Voce equation [38–41], the intercept of the best fittng line gives information on the integrity of the tested material. Considering the data of samples with a Si content of 3.5 wt.% [15], the intercept is positive. Thus, σ_V grows with increasing Θ_o. The latter is correlated to the microstructure of the material: complying with plasticity theory, greater values of Θ_o (thus σ_V) are associated to finer microstructure and so to a stronger materials as demonstrated in a previous study [42, 43] on GJS400 with a conventional Si content of 2.5 wt.%.

However, according to Figure 3, samples with a Si content of 4.2 wt.% up to 4.5 wt.% show corresponding best fitting line with a negative intercept value that decreases with increasing the Si content. Remembering the aforesaid definition of saturation stress σ_V, the negative value of the intercept C results in a reduction of σ_V increasing Θ_o. This result is in contrast with Voce physical meaning and plasticity theories. It has been reported [44] that the presence of defects affects the plastic behavior of the material describing an unexpected regular trend, i.e. *defect-driven plasticity*, rather than a random influence as expected.

In Figure 4, data of HSiSDI samples with 4.2 wt.% Si content are reported comparing Lynchburg and Y-block molds. According to MAD, specimens produced through small thickness (25 mm Lynchburg and Y-block molds) show a positive intercept of the best fitting line. On the other hand, samples produced with 50–75 mm Y-molds show a negative intercept, so suggesting that the HSiSDIs produced with faster cooling rates is sound, while with slower cooling rates the material is affected by defects according to the defects-driven-plasticty hypothesis.

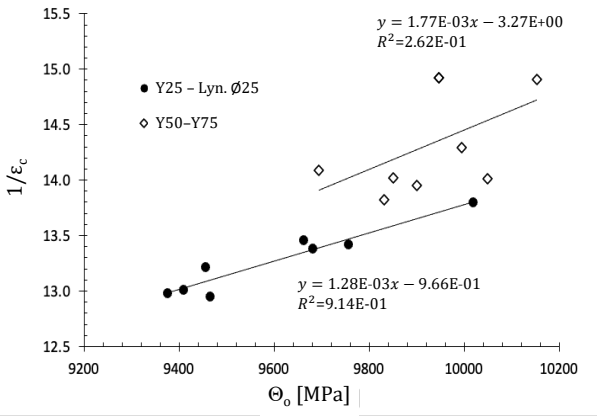

Fig. 4. Matrix Assessment Diagram (MAD) of HSiSDIs with Si content of 4.2 wt.% produced through Lynchburg and Y-block molds

Figure 5 reports the Integrity Assessment Diagram (IAD), defined as $\varepsilon_{rupture}$ vs. $\varepsilon_{uniform}$. The dashed line represents the dicotomy line, where $\varepsilon_{rupture} = \varepsilon_{uniform}$, and defines the occurrence of necking. The data points where $\varepsilon_{rupture} < \varepsilon_{uniform}$ are related to early failures due to the presence of metallurgical defects or metallurgical discontinuity, while the points where $\varepsilon_{rupture} > \varepsilon_{uniform}$ are related to sound materials. Specimens with 4.2 wt.% Si produced through 25 mm Lyncburg and Y-molds lie above the dicotomy line, so beyond necking, and show a mean value of elongation to rupture of 0.16 ±0.01, where the error is the standard deviation. Decrasing the cooling rates (50–75 mm Y-blocks), in IAD it is observed a certain variability of the data, which seems to be related to the soundness of the material. Furthermore, compared to 25 mm samples, these data show a reduction of the elongation to rupture to an average value of 0.11 ±0.04 that, evidently, is not due to the high Si content which remain unchanged between the specimens. Thus the key role of the possible presence of metallurgical defects on the definition of the tensile plastic behavior of the material under analysis can be confirmed.

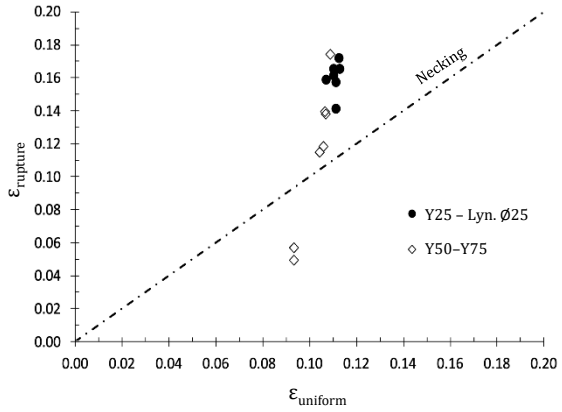

Fig. 5. Integrity Assessment Diagram (IAD) of HSiDIs with 4.2 wt.% Si produced through Lynchburg and Y-block molds

4. DISCUSSION

In the present investigation, HSiSDI samples with a Si content of 4.2 wt.% produced through different molds, so with different cooling rates, were analyzed. According to Figure 2 and the data reported in Table 2, the graphite parameters were consistent to the values found for Si 3.5 wt.% and 4.5 wt.% reported elsewhere [15]. Nodularity was good for all cooling rates, with a slightly lower value for the Lynchburg mold, suggesting that no significant graphite degeneracy was present for all solidification times. In fact chunky graphite was found in traces only for the slower cooling rates (50–75 mm Y-blocks), consistently with literature [4, 25–27] where it has been reported that Si and slow solidification rates promote the formation of chunky graphite.

According to Figure 3, where data of the present research were compared with the results of a previous study [15] on other two HSiSDIs with different Si contents, MAD can identify the different grades of ductile iron since three different lines corresponding to three different contents of Si are found. MAD can give information also about the microstructure soundness of the materials, which is correlated to the plastic behavior according to the defect-drive-plasticity theory. Specimens with a Si content of 3.5 wt.% [15] show a fitting line having a positive intercept (C = +2.54), indicating soundness of the material [39–45]. Conversely, for a Si content of 4.5 wt.% [15], the intercept of the best fitting line is negative (C = −4.43), suggesting the presence of chunky graphite as reported in [15]. So, according the the defect-driven-plasticity hypotesis, the negative intercept (C = −3.27) of the Si 4.2 wt.% suggests the presence of some defects.

In Figure 4, a close up of 4.2 wt.% Si MAD data is reported. For longer solidification times, i.e. Y50-75 mm, not only the intercept of the linear fit is negative (C = −3.27), but the data show also a significant scattering and low R^2, equal to 0.26. Furthermore, the data corresponding to the faster cooling rates (25 mm Lynchburg and Y-block) show a positive intercept (C = +0.97) of the best fitting line, suggesting the soundness of the material. It is noteworthy that the behaviour observed is absolutely consistent with the MAD trend of Si 4.5 wt.% samples reported in [15], which was related to

significant fraction of chunky graphite found in the HSiSDIs produced with slow cooling rates.

The IAD in Figure 5 shows that the microstructure of samples produced through 25 mm Lynchburg and 25 mm Y-block molds, have higher strains to failure with respect the values of 50–75 mm Y-blocks specimens. Furthermore, since $\varepsilon_{rupture} > \varepsilon_{uniform}$, it is newly suggested the integrity of the material, whilst for 50–75 mm Y-blocks specimens not all data are above the dichotomy line of necking. This finding indicates that some defects are present in the HSiSDIs produced with longer solidification time, which is consistent with the negative value of the intercept C in MAD. By comparing these findings with the results of Si 4.5 wt.% HSiSDIs reported in [15], where significant content of chunky graphite was found, the analogy is very strong, suggesting that the defects that most define the Si 4.2 wt.% behaviour in MAD are the traces of chunky graphite. Indeed, several data points are above the dichotomy line, suggesting the absence of defects and a good plastic behaviour. So the traces of chunky graphite give rise to a wide variability of MAD behaviour. So the unpredictability of the HSiSDIs with 4.2 wt.% Si produced with slower cooling rates may be a negative consequence.

So the presence in traces of chunky graphite have some negative effects on the quality of Si 4.2 wt.% HSiSDIs produced with longer solidification times (Y-molds of 50–75 mm thickness). The quality assessment procedure based on Voce analysis (MAD and IAD) seems to be very sensitive and capable of identifying its adverse effects even if the microstructure parameters reported in Table 2 comply with standard EN 1563:2018. Indeed, chemical ordering is also believed to be deleterious in HSiSDIs with increasing Si [7, 8]. However, since there is no reason to believe that cooling rates can affect chemical ordering, chunky graphite appears to be the reliable explanation of the defect-driven-plasticity effects pointed out in MAD and IAD for HSiSDIs with Si content of 4.2 wt.%.

5. CONCLUSIONS

In the present work different samples of HSiSDI with a Si content of 4.2 wt.%, produced through different molds, thus different solidification rates, were studied in order to evaluate the correlation between the microstructure and the tensile mechanical properties through Voce analysis. Four different cooling rates were explored to produce the HSiSDIs. The microstructural characterization was performed using a high resolution SEM and the image analysis was conducted complying standard ASTM E2567-16a. The tensile mechanical behavior was investigated according to Voce approach, so modelling the tensile flow curves through Voce constitutive equation. Voce parameters $1/\varepsilon_c$ and Θ_o were determined and used to define the MAD. Furthermore, it was possible to define the IAD that allows to identify the eventual premature failures of the tensile tested materials. According to the experimental results obtained, the following consideration can be made:

- MAD allows the univocal identification of the tested material since, through the comparison with result of a previous study [15], three different best fitting lines corresponding to three different contents of Si are found;
- the intercept of the data best fitting line in MAD of the 25 mm Lynchburg and 25 mm Y-block samples with a Si content of 4.2 wt.% is positive, according to Voce equation physical meaning and plasticity theories. So, the tensile plastic behavior observed comply with the fact that increasing σ_V and σ_0 determine an increment of Θ_o, which is correlated to the microstructure of the material;
- the negativity of the intercept of the data best fitting line in MAD of 50–75 mm Y-blocks specimens is not coherent with physical meaning of Voce equation and plasticity theories, with the result of a singular tensile mechanical behavior for which decreasing σ_V determines an increase of Θ_o with σ_0 constant;
- the MAD data of Y50–Y75 mm samples, i.e. those produced through the slowest cooling rates, show a significant scattering with low R^2. Furthermore, these specimens show a reduction of the elongation to failure and, in some cases, premature ruptures occurred before necking;
- according to IAD, data of specimens produced through 25 mm Lynchburg and Y-block molds, lie beyond necking; thus premature ruptures did not occur;
- the plastic behavior shown by 25 mm Lynchburg and 25 mm Y-block samples is correlated to the optimal structural integrity of the microstructure;
- the unusual behavior of 50–75 mm Y-block samples was affected by the presence of metallurgical defects, in particular by the presence of degenerated graphite;
- considering the results obtained, it can be stated that the quality assessment procedure based on the Voce approach is clearly sensitive and capable of identifying the presence of defects and metallurgical discontinuities; furthermore, this procedure has proved capable of highlighting the negative effects of such defects on the quality of the material and thus demonstrating its usefulness.

REFERENCES

[1] Weiβ P., Brachmann J., Bührig-Polaczek A. & Fischer S.F. (2015). Influence of nickel and cobalt on microstructure of silicon solution strengthened ductile iron. *Materials Science and Technology*, 31(12), 1479–1485. Doi: https://doi.org/10.1179/1743284714Y.0000000735.

[2] de la Torre U., Loizaga A., Lacaze J. & Sertucha J. (2014). As cast high silicon ductile irons with optimised mechanical properties and remarkable fatigue properties. *Materials Science and Technology*, 30(12), 1425–1431. Doi: https://doi.org/10.1179/1743284713Y.0000000483.

[3] Sertucha J., Lacaze J., Serrallach J., Suárez R. & Osuna F. (2012). Effect of alloying on mechanical properties of as cast ferritic nodular cast irons. *Materials Science and Technology*, 28(2), 184–191. Doi: https://doi.org/10.1179/1743284711Y.0000000014.

[4] Stets W., Löblich H., Gassner G. & Schumacher P. (2014). Solution strengthened ferritic ductile cast iron properties, production and application. *International Journal of Metalcasting*, 8(2), 35–40. Doi: https://doi.org/10.1007/BF03355580.

[5] Björkegren L.E., Hamberg K. & Johannesson B. (1996). Mechanical properties and machinability of Si-solution-hardened ferritic ductile iron. *AFS Transactions*, 104, 139–145.

[6] Khalil-Allafi J. & Amin-Ahmadi B. (2011). Influence of mold preheating and silicon content on microstructure and casting properties of ductile iron in permanent mold. *Journal of Iron and Steel Research International*, 18(3), 34–39. Doi: https://doi.org/10.1016/S1006-706X(11)60034-4.

[7] González-Martíneza R., de la Torre U., Lacaze J. & Sertucha J. (2018). Effects of high silicon contents on graphite morphology and room temperature mechanical properties of as-cast ferritic ductile cast irons. Part I – Microstructure. *Materials Science Engineering: A*, 712, 794–802. Doi: https://doi.org/10.1016/j.msea.2017.11.050.

[8] González-Martínez R., de la Torre U., Ebelb A., Lacaze J. & Sertucha J. (2018). Effects of high silicon contents on graphite morphology and room temperature mechanical properties of as-cast ferritic ductile cast irons. Part II – Mechanical properties. *Materials Science Engineering: A*, 712, 803–811. Doi: https://doi.org/10.1016/j.msea.2017.11.051.

[9] Bradley W.L. & Srinivasan M.N. (1990). Fracture and fracture toughness of cast irons. *International Materials Reviews*, 35(1), 129–161. Doi: https://doi.org/10.1179/095066090790324028.

[10] Angus H.T. (1976). Cast Iron: Physical and Engineering Properties (Second Edition). Butterworth-Heinemann.

[11] Lacaze J., Larrañaga P., Asenjo I., Suárez R. & Sertucha J. (2012). Influence of 1 wt% addition of Ni on structural and mechanical properties of ferritic ductile irons. *Materials Science and Technology*, 28(5), 603–608. Doi: https://doi.org/10.1179/1743284711Y.0000000100.

[12] Alhussein A., Risbet M., Bastien A., Chobaut J.P., Balloy D. & Favergeon J. (2014). Influence of silicon and addition elements on the mechanical behavior of ferritic cast iron. *Materials Science Engineering: A*, 605, 222–228. Doi: https://doi.org/10.1016/j.msea.2014.03.057.

[13] Glavas Z., Strkalj A. & Stojakovich A. (2016). The properties of silicon alloyed ferritic ductile irons. *Metalurgija*, 55(3), 293–296.

[14] Fairhurst W. & Röhrig K. (1979). High-silicon nodular irons. *Foundry Trade Journal*, 146, 657–681.

[15] Angella G., Donnini R. & Zanardi F. (2020). Assessment of microstructure effects on tensile behaviour in silicon strengthened ductile irons produced through different cooling rates. *International Journal of Cast Metals Research*, 33(2–3), 89–102. Doi: https://doi.org/10.1080/13640461.2020.1757917.

[16] Karsay S.I. & Campomanes E. (1970). Control of graphite structure in heavy ductile iron castings. *AFS Transactions*, 78, 85–92.

[17] Lacaze J., Magnusson-Åberg L. & Sertucha J. (2013). Review of microstructural features of chunky graphite in ductile cast irons. Keith Millis World Symposium on Ductile Cast Iron: 15–17 October, Nashville. Red Hook (NY): Curran, 360–368.

[18] de la Torre U., Lacaze J. & Sertucha J. (2016). Chunky graphite formation in ductile cast irons: effect of silicon, carbon and rare earths. *International Journal of Materials Research*, 107(11), 1041–1050. Doi: https://doi.org/10.3139/146.111434.

[19] Bauer B., Pokopec I. M., Petrič M. & Mrvar P. (2017). Effect of Si and Ni addition on spheroidal morphology in heavy section spheroidal graphite iron parts. *Materials Science Forum*, 925, 70–77. Doi: https://doi.org/10.4028/www.scientific.net/MSF.925.70.

[20] Gagné M. & Argo D. (1987). Heavy section ductile iron castings – Part I: Structure and properties. Advanced Casting Technology: 12–14 November, Kalamazoo. ASM International, 231–244.

[21] Källbom R., Hamberg K. & Björkegren L.E. (2005). Chunky-graphite – formation and influence on mechanical properties in ductile cast iron. In: J. Samuelson, G. Marquis, J. Solin (Eds.). Competent Design by Castings: Improvements in a Nordic Project, 13–14 June. Espoo. Helsinki.

[22] Celis M.M., Domengès B., Hug E. & Lacze J. (2018). Analysis of nuclei in a heavy-section nodular iron casting. *Materials Science Forum*, 925, 173–180. Doi: https://doi.org/10.4028/www.scientific.net/MSF.925.173.

[23] Minnebo P., Nilsson K.F. & Blagoeva D. (2007). Tensile, compression and fracture properties of thick-walled ductile cast iron components. *Journal of Material Engineering and Performance*, 16(1), 35–45. Doi: https://doi.org/10.1007/s11665-006-9005-z.

[24] Borsato T., Ferro P., Berto F. & Carollo C. (2016). Mechanical and fatigue properties of heavy section solution strengthened ferritic ductile iron castings. *Advanced Engineering Materials*, 18(12), 2070–2075. Doi: https://doi.org/10.1002/adem.201600256.

[25] Goodrich G.M. & Lobenhofer R.W. (2002). Effect of cooling rate on ductile iron mechanical properties. *AFS Transactions*, 110, 1003–1032.

[26] Hsu G.H., Chen M.L. & Hu C.J. (2007). Microstructure and mechanical properties of 4% cobalt and nickel alloyed ductile irons. *Materials Science Engineering: A*, 444 (1–2), 339–346. Doi: https://doi.org/10.1016/j.msea.2006.09.027.

[27] Serrallach J., Lacaze J., Sertucha J., Suárez R. & Monzón A. (2011). Effect of selected alloying elements on mechanical properties of pearlitic nodular cast irons. Key Engineering Materials, 457, 361–366. Doi: https://doi.org/10.4028/www.scientific.net/KEM.457.361.

[28] Tartaglia J.M., Gundlach R.B. & Goodrich G.M. (2014). Optimizing structure-property relationships in ductile iron. *International Journal of Metalcasting*, 8 (4), 7–38. Doi: https://doi.org/10.1007/BF03355592.

[29] Ceschini L., Morri Al., Morri An., Salsi E., Squatrito R., Todaro I. & Tomesani L. (2015). Microstructure and mechanical properties of heavy section ductile iron castings: experimental and numerical evaluation of effects of cooling rates. *International Journal of Cast Metals Research*, 28(6), 365–374. Doi: https://doi.org/10.1179/1743133615Y.0000000022.

[30] Zanardi F., Bonollo F., Bonora N., Ruggiero A. & Angella G. (2017). A contribution to new material standards for Ductile Irons and Austempered Ductile Irons. *International Journal of Metalcasting*, 11(1), 136–147. Doi: https://doi.org/10.1007/s40962-016-0095-6.

[31] Ductile Iron Data for Design Engineers – Section III. Engineering Data (Part 1) Tensile Properties: Relationships between Tensile Properties. Retreived from: https://ductile.org [accesed 13 July 2019].

[32] Rivera G., Boeri R. & Sikora J. (2003). Influence of the inoculation process, the chemical composition and the cooling rate, on the solidification macro and microstructure of ductile iron. *International Journal of Cast Metals Research*, 16 (1–3), 23–28. Doi: https://doi.org/10.1080/13640461.2003.11819553.

[33] Stefanescu D.M., Ruxanda R. & Dix L.P. (2003). The metallurgy and tensile mechanical properties of thin wall spheroidal graphite irons. *International Journal of Cast Metals Research*, 16(1–3), 319–324. Doi: https://doi.org/10.1080/13640461.2003.11819602.

[34] Pan Y.-N., Lin C.-C. & Chang R.-M. (2012). Assessments of relationship between microstructures and mechanical properties for heavy section ductile cast irons. *International Journal of Cast Metals Research*, 25(5), 301–306. Doi: https://doi.org/10.1179/1743133612Y.0000000027.

[35] Donnini R., Zanardi F., Vettore F. & Angella G. (2018). Evaluation of microstructure quality in ductile irons based on tensile behaviour analysis. *Materials Science Forum*, 925, 342–349. Doi: https://doi.org/10.4028/www.scientific.net/MSF.925.342.

[36] Angella G. & Zanardi F. (2018). Microstructure quality assessment of isothermed ductile irons through tensile tests. 73rd World Foundry Congress "Creative Foundry": 23–27 September. Krakow. Krakow: Stowarzyszenie Techniczne Odlewników Polskich, 265–266.

[37] Angella G. & Zanardi F. (2019). Validation of a New Quality Assessment Procedure for Ductile Irons Production Based on Strain Hardening Analysis. *Metals*, 9(8), 837–850. Doi: https://doi.org/10.3390/met9080837.

[38] Estrin Y. (1996). Dislocation density related constitutive modelling. In: A. Krausz, K. Krausz, Unified Constitutive Laws of Plastic Deformation, 1. New York: Academic Press, 69–106.

[39] Kocks U.F. & Mecking H. (2003). Physics and phenomenology of strain hardening: the FCC case. *Progress in Materials Science*, 48(3), 171–273. Doi: https://doi.org/10.1016/S0079-6425(02)00003-8.

[40] Angella G., Zanardi F. & Donnini R. (2016). On the significance to use dislocation-density-related constitutive equations to correlate strain hardening with microstructure of metallic alloys: The case of conventional and austempered ductile irons. *Journal of Alloys and Compounds*, 669, 262–271. Doi: https://doi.org/10.1016/j.jallcom.2016.01.233.

[41] Angella G. & Zanardi F. (2018). Comparison among Different Constitutive Equations on Investigating Tensile Plastic Behavior and Microstructure in Austempered Ductile Iron. *Journal of Casting & Materials Engineering*, 2(1), 14–23. Doi: https://doi.org/10.7494/jcme.2018.2.1.14.

[42] Angella G., Masaggia S., Ripamonti D., Górny M. & Zanardi F. (2019). The role of microstructure on tensile plastic behaviour of ductile iron GJS 400 produced through different cooling rates, Part I: Microstructure. *Metals*, 9(12), 1282. Doi: https://doi.org/10.3390/met9121282.

[43] Angella G., Donnini R., Ripamonti D., Górny M. & Zanardi F. (2019). The role of microstructure on tensile plastic behaviour of ductile iron GJS 400 produced through different cooling rates, Part II: Tensile Modelling. *Metals*, 9(9), 1019. Doi: https://doi.org/10.3390/met9091019.

[44] Angella G., Cova M., Berutzzi G. & Zanardi F. (2020). Soundness Discrimination in Ferrite Ductile Irons through Tensile Data Analysis. *International Journal of Metalcasting*, 14(3), 816-826. Doi: https://doi.org/10.1007/s40962-020-00435-0.

[45] Estrin Y. (1998). Dislocation theory based constitutive equation modelling: foundation and application. *Journal of Materials Processing and Technology*, 80–81, 33–39. Doi: https://doi.org/10.1016/S0924-0136(98)00208-8.

Journal of Casting & Materials Engineering Vol. 6 No. 1 (2022) 8–13
https://doi.org/10.7494/jcme.2022.6.1.8

An Analysis of the Features of Cast Composite Materials Based on Light Alloys Reinforced by Particles

Olena Dan[a,b]

[a] AGH University of Science and Technology, Faculty of Foundry Engineering, al. A. Mickiewicza 30, 30-059 Krakow, Poland
[b] MDPI Branch Office Kraków, al. Jana Pawła II 43a, 31-864 Krakow, Poland
e-mail: danelena.leo@gmail.com

Received: 24 June 2021/Accepted: 21 December 2021/Published online: 14 January 2022.
This article is published with open access at AGH University of Science and Technology Journals.

Abstract

Light alloys are widely used in industry and everyday life due to their high physical and mechanical properties, wear and corrosion resistance, as well as low cost. In this regard, the use of light alloys as a basis for composite materials is both justified and expedient. The potential of these materials has not been fully used to this day, despite the growing interest in metal matrix composites and extensive investigations aimed at the development of production technology and the introduction of advanced systems based on light matrices. The article presents a short review of the analysis of the main components of the technology of cast composite materials based on light alloys of aluminum and magnesium reinforced by particles. Particular attention is paid to the choice of the matrix alloy, the type, size and amount of reinforcing particles introduced into it, as well as the thermal-time and kinetic parameters of the process.

Keywords:
aluminium, magnesium, alloy, composite material, matrix, reinforcing particles

1. INTRORODUCTION

The successful functioning and further development of most modern industries, such as aerospace, transport, military, biomedicine, is impossible without the use of lightweight, durable and inexpensive materials in manufacturing [1–3]. Today, all these requirements are met by composite materials (CM) based on Al and Mg alloys [4–6].

Composite materials are materials containing two or more phases (matrix and reinforcing phase), significantly different in properties and having a clear interface [7]. The properties of the finished composite material are superior to those of its constituent components. Highly plastic metal matrices, for example, aluminium alloys, and high-strength, high-modulus fillers are artificially combined in CM. It is possible to obtain composites with such combination of phases with the required values of strength, elastic modulus, microhardness, crack and heat resistance as well as to create compositions with the required dielectric, magnetic, radio-absorbing and other special characteristics [8, 9].

Depending on the type of reinforcement, composites are divided into [9]: fibrous composites, particle reinforced composites, sandwich composites, hybrid composites.

The advantages of particle reinforcement are [10] significantly lower cost of the composite compared to the continuous fiber reinforcement (cheaper production of the composite; cheaper reinforcement), the possibility of producing them with metallurgical methods (casting or powder metallurgy) as well as properties similar to isotropic.

Globally, the data presented in [2] shows that primary Al production increased by approximately 1.5 times from 2009 to 2019. According to the Global Metal Matrix Composites Market Report, in the same period there has been linear growth in the production of metal matrix composites after 2012, and revenue has increased from about 220 million USD to 400 million USD [11].

The main focus when obtaining CM should be paid to the selection of both the matrix alloy and its reinforcing particles. The matrix alloy must be uniform, strong, lightweight, and inexpensive. The particles must have a high degree of hardness and be evenly distributed in the matrix, as well as reliably fixed in it. Only in this case will a positive technical and economic result be achieved.

The aim of this study is to analyze the production technologies, the influence of various characteristics of the matrix and reinforcing particles on the properties of cast composite materials (CCM) based on light (aluminium and magnesium) alloys.

2. ALUMINIUM AND MAGNESIUM MATRIX COMPOSITE MATERIALS

The most commonly used metals as a matrix for composites are aluminum, magnesium and titanium, with copper and

zinc and their alloys less frequently employed [12]. According to [1, 2, 7, 13] composite materials based on the light alloys make up the bulk of the CCM currently produced.

Among all metal matrix composites, aluminum composites constitute a large and important group of construction materials. Since the matrix of the composite has many functions, it is important to select the appropriate alloy to ensure optimal properties and compatibility with the reinforcement. Aluminum alloys have low density, high specific strength and a relatively low price, therefore they are an attractive construction material. Magnesium and its alloys are very attractive matrix materials due to their very low density (1.74 g/cm^3), however they are much more susceptible to corrosion than aluminum alloys. In addition to pure magnesium, alloys of magnesium with aluminum, manganese, zinc and strontium are used in the production of composites. The above-mentioned alloy additives improve, among others, castability, strength and corrosion resistance. The most commonly used alloys are AZ91, AJ62 and AM50 [14].

Alloys based on Al and Mg have the high physical and mechanical properties, wear and corrosion resistance, as well as low cost, that's why they are widely used for purposes of industry and everyday life. At the same time, it is obvious that today's requirements for the parts of machines and mechanisms cannot be satisfied by even the whole variety of known alloys. A way out can be found by creating CM using a metal matrix on an aluminum and magnesium base.

Such materials are promising for use as thermal barrier coatings for blades of gas turbine engines, cryogenic flanges and other high-pressure elements of liquid-propellant rocket engines, lightweight pipelines in aviation and space technology, housings for electronic equipment, static and moving parts of electronic equipment [1, 15].

In addition, metal-matrix aluminium composites are currently used as radiation-shielding materials. Firstly, it is the protection of equipment and machinery operating in conditions of radiation damage. Secondly, it is a biological protection of personnel serving this equipment and machinery at nuclear facilities, as well as personnel of medical and emergency rescue services with increased requirements for biologically inert and X-ray protective properties of materials. A new class of lightweight radiation-shielding materials based on aluminium and magnesium composites with various ceramic fillers, depending on the type of ionizing radiation, is being developed. Such materials have high mechanical properties, but operating in the mode of increased ionizing radiation, they are subject to significant swelling, including due to structural changes. These structural changes can be prevented by using metals that are less susceptible to swelling and modification with various nanostructure fillers [16].

3. METHODS FOR OBTAINING COMPOSITE MATERIALS

All methods for obtaining composite materials are usually divided into solid-state, liquid-state and gas-state [7, 9, 13, 17, 18]. Liquid-phase methods are more technological and less expensive than solid-state (e.g., powder metallurgy methods, equi-channel angular pressing, etc.) due to the fact that most liquid-state methods are associated with the production of CM based on low-melting alloys. Methods of impregnation and casting are the most common liquid-phase methods.

The matrix metal, which is in a completely or partially molten state during the implementation of liquid-state methods, is mixed with the reinforcing material, forming a composite material that is new in its properties. In addition to other advantages, this approach to the production of CM makes it possible to effectively control the processes occurring at the interface between the solid and liquid phases.

The properties of the resulting composite material depend on a number of parameters (Fig.1).

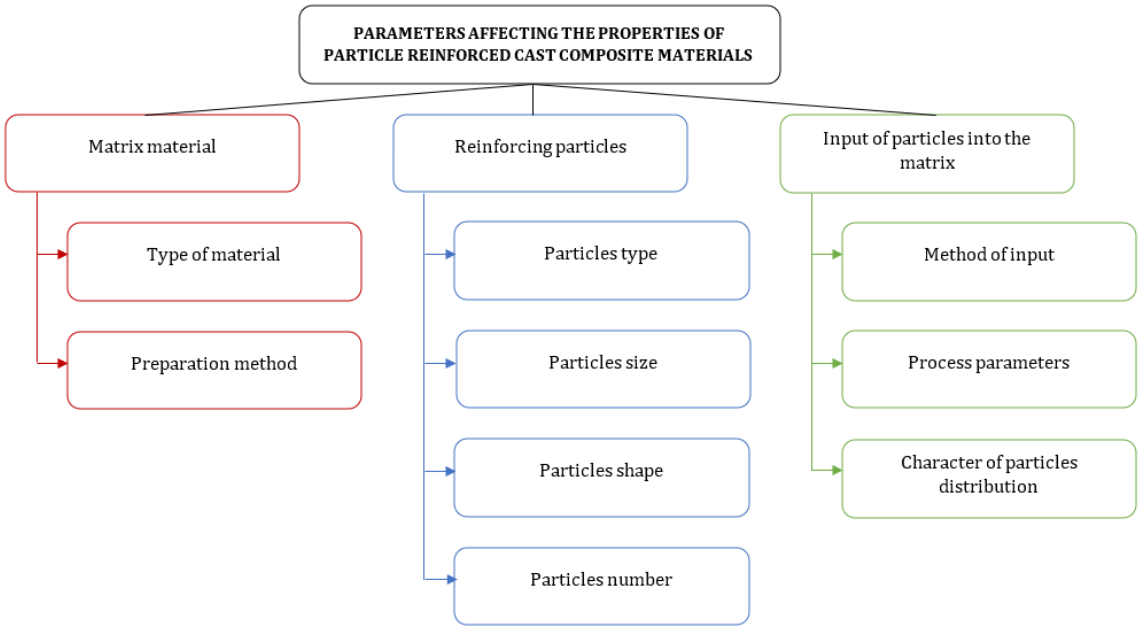

Fig. 1. Parameters affecting the properties of particle reinforced cast composite materials

4. REINFORCING PARTICLES AND THEIR INTERACTION WITH LIQUID METAL IN COMPOSITE MATERIALS

In the technology of producing CCM it is important to choose a reinforcing material and a method of introducing reinforcing particles into the melt in addition to the choice of a matrix alloy. The reinforcing particles characteristics determine the vector of properties changes of the base material. The price of the finished product is also important, given its performance characteristics.

Depending on the nature and material composition of the introduced particles, they can contribute to an increase in the strength, friction, or antifriction characteristics of the matrix alloy. The properties of CCM reinforced with solid, insoluble, refractory particles are largely determined by the nature, size, volume fraction, shape of these particles and their interaction with the matrix. Common to most production methods is the reinforcement of matrix alloys with a dispersed phase in the form of particles of oxides, nitrides, carbides, borides, and refractory metals [14, 19]. Finely dispersed materials obtained from industrial wastes are increasingly wider lately used as technologically and economically acceptable reinforcing elements for products based on matrices of aluminum alloys [20]. Slags of metallurgical production and cupola smelting, enrichment wastes, ash from thermal units, fireclay powders, broken ceramics, etc., which are ground into powder in ball or vibration mills and calcined in drying ovens or in chamber furnaces are used. There are known cases of introduction of particles of graphite and/or bronze in the form of chips to increase the antifriction properties of Al alloys [8, 21]. Particles of SiC, Al_2O_3, B_4C, cast basalt fibers, graphite flakes and mica are quite often introduced into alloys based on Al and Mg [6, 22, 23].

The micro-particles size can vary within wide limits from 0.1 to 400 μm [6, 7, 24–28]. In recent years, a too large number of studies have been devoted to the reinforcement of aluminium matrices with nanoparticles from 10 to 1000 nm [15, 18, 29–32].

Reinforcements in the form of fibres or particles can be a hardening phase only in the case of high interfacial adhesion. Typically, poor wetting is noted in the melt-solids combinations used. Improving the wetting of solid particles by liquid metal enhances their bond with the matrix metal, thereby increasing the mechanical and operational characteristics of finished products. The introduction of surface-active elements into the liquid metal reduces the surface tension at the interface between the solid and liquid phases. Heating and sometimes calcining of the reinforcing particles before being introduced into the liquid matrix alloy is necessary to remove moisture and other gases adsorbed by the surface from their surface. The positive effect of heating the particles is also reflected in the improvement of their wettability. An increase in the temperature of the melt during the introduction of dispersed particles into it has a similar effect on improving wetting.

It is possible to obtain a pure matrix metal, and to ensure its reliable contact with reinforcing particles using an inert gas or vacuum instead of an oxidizing atmosphere in the process of obtaining CM.

The amount of solid phase introduced into the melt when implementing liquid-state methods is usually less under implementing solid-state methods [13]. There are no universal recommendations in the literature on the amount of injected particles. There can be no such recommendations, since the amount of the dispersed phase, providing the greatest increase in the level of various properties, depends on the nature of the matrix alloy and solid particles, their size and the nature of their distribution in the matrix. So with the introduction of even 0.3–1.0 wt.% WS_2 with a fraction of ~2 μm, a noticeable increase in the ultimate strength and yield strength of the AZ91 alloy was noted [33]. The authors [34] found a positive effect on the compressive and tensile strength even with the introduction of 1.0 wt.% B_4C particles into a matrix of AZ91 alloy. In study [25] it was found that for the combination AZ91/SiC_p with a particle size of 20–40 μm, the optimal amount of solid phase is about 10–15 wt.% for increasing of strength properties. In [4], a significant increase in the wear resistance of the AZ91 alloy was noted when reinforcing it with 10 wt.% particles of SiC_p with an average grain size of 10 μm. According to the results of investigations [35], it is recommended to introduce 5–50 vol.% solid particles into high-alloy steels in the form of carbides, titanium nitrides, tungsten and niobium in order to increase the wear resistance of cast parts.

It is shown in [36, 37] that with a high volume fraction of reinforcing particles, CM with an aluminium matrix shows high contact strength, that's why they can be used to create supporting elements of cargo roller tables, mirrors substrates for guidance systems and parts of hydraulic devices.

There is little discussion in the literature about the influence of the shape of reinforcing particles on the properties of CCM. As a rule, particles of ceramics, carbides, metal nitrides have an acute-angled, chipped shape, graphite particles are lamellar, and refractory metals are rounded [5, 7, 35]. It is obvious that the shape of dispersed particles can be a factor that determines the different characteristics of the finished CM. For considering this issue an analogue can be the form of graphite in cast iron [38]. It has been established that inclusions of lamellar graphite in gray cast iron have a notching effect on the metal matrix, in contrast to inclusions of nodular graphite in ductile iron. As a consequence, ductile iron has a much higher level of mechanical properties. It should be assumed that inclusions of rounded solid particles will be more favourable for the properties of CCMs compared to acute-angled or splintered ones.

It is necessary to consider the role of dispersed particles in crystallization processes. The rate of crystals nuclei formation as well as the rate of their growth, are two competing processes that ultimately determine the micro- and macrostructure of the solidified metal base, and, consequently, the complex of its properties. Thus, the predominance of the rate of formation of embryos over the rate of their growth leads to the appearance of a fine-grained micro- and macrostructure and a higher level of properties, in comparison with the opposite case [39].

Dispersed reinforcing particles can become heterogeneous nuclei of crystallization. At the same time, there is an opinion that the introduction of dispersed refractory fillers into

aluminium melts helps to reduce the dendritic parameter of the cast structure. Ceramic particles, according to [40], are not crystallization centres, but are pushed aside by growing dendrites of α-aluminium into interdendrite spaces enriched with easy-melting phases. The modifying role of ceramic particles is due to the limitation of the volumes of the melt in which the liquation takes place. Particles of metal-like carbides and intermetallic compounds also have a modifying effect on the cast structure of CM, but already as crystallization centres. When graphite particles are added to the CM composition, the particles are located mainly in the interdendrite spaces and can also serve as a substrate for primary silicon crystals in Al-Si alloys. It was found that the refinement of the fragments of the structure increases with an increase in the content of ceramic and graphite particles in the CM.

5. METHODS OF INTRODUCING REINFORCING PARTICLES INTO THE MELT AND PARAMETERS OF THE INJECTION PROCESS

The next parameter of the CM manufacturing technology by liquid-state methods is that of introducing solid particles into the liquid phase. Depending on the chosen method, several variants of the distribution of particles in the matrix can be obtained. One of the following input methods can be selected depending on the expected result.

The most common is the stirring method, designed to ensure the uniform dispersion of reinforcing particles [5, 7, 29, 33, 41]. The basic principle of the method is the reinforcing particles are introduced directly into the molten matrix metal and are evenly distributed in it due to stirring. The more uniformly the hard particles are distributed in the soft matrix, the higher the level of properties in the entire volume the resulting composite acquires. Therefore, it is important to choose the right technological parameters of the process:

- stirring speed;
- stirring time;
- melt temperature;
- heating temperature of the introduced particles;
- the introduction of wetting agents into the melt.

The stirring rate is an extremely important parameter that determines the degree of turbulence of the liquid metal flow, and, consequently, the nature of the distribution of solid particles in the melt. As shown in [5, 7, 41], the movement of reinforcing particles in molten metal is directly related to the speed of its movement. In this case, the higher the mixing rate is higher the degree of flow turbulence and the less noticeable sedimentation processes, the more uniformly the particles are distributed in the liquid and then in the solidified matrix alloy. In the same works, it was shown that with an increase in the mixing rate, the surface tension at the interface between the solid and liquid phases decreases, which, as already noted, is very important for ensuring reliable fixation of particles in the matrix. In practice, high-speed mechanical with a rotation frequency of up to 4000 rpm and more and ultrasonic mixers are used for mixing reinforcing particles into liquid metal [42]. The choice of stirring speed should be based on an estimate of the melt viscosity. This parameter is known to be directly related to the composition of the liquid metal and its temperature.

Stirring time is also a critical process parameter [43]. An insufficient stirring time can lead to the uneven distribution of solid particles in the liquid metal, their concentration in some volumes and absence in others. Excessive stirring can result in deformation and destruction of the active element of the agitator due to high temperatures combined with mechanical stress. Obviously, it is necessary to empirically choose the optimal stirring time for each specific case.

The choice of the process temperature is an important element of the castings manufacturing technology from CM [44]. The function of temperature is fluidity to providing the required viscosity of the melt at the time of introducing and mixing reinforcing particles in it. The role of fluidity in filling moulds and obtaining the correct configuration of castings is widely recognized. An increase in the temperature of the melt, in addition, improves the wetting of dispersed particles by the melt.

A slightly different approach to ensuring a uniform distribution of reinforcing particles is implemented under casting by the lost-foam method. Solid particles are mixed with granules of expanded polystyrene and injected into a compression mould [45, 46]. Their uniform distribution in the model is preserved in the finished casting. This method has not yet found wide application in practice due to poor process control.

The second option is typical for obtaining functional-gradient materials. In this case, the necessary parameters of physical properties and performance characteristics (coefficients of friction, thermal expansion, wear resistance, elastic modulus, etc.) are implemented in separate specified areas of the product. Reinforcing particles in one way or another are concentrated in the most loaded section of the casting, thereby increasing its efficiency. There are several ways of such concentration. The production of composites by centrifugal casting makes it possible to obtain blanks with a differentiated distribution of reinforcing elements over the section of the casting [47]. The resulting parts have a reinforced outer or inner surface (zone), depending on the ratio of the density of particles and matrix alloy [8, 47–49]. One of the most important technological factors in centrifugal casting, affecting segregation processes, is the gravitational coefficient, showing how many times all the components of the alloy become heavier in the field of action of centrifugal forces.

During casting in stationary moulds, due to the difference in the specific gravity of the matrix metal and reinforcing particles, they can be concentrated either in the upper or in the lower part of the casting, thereby giving it the necessary properties that differ from those of the base metal.

Another group of methods for introducing reinforcing particles into a matrix alloy is based on the technology proposed by Nukami and Flemings [50]. *In-situ* technology, is based on the synthesis of the second phase as a result of the chemical interaction of the components introduced into the melt. It is characterized by a number of advantages:

- simple and relatively inexpensive equipment;
- short technological cycle;
- high purity and quality of the final alloys.

The most widespread technology option is the preparation of a master alloy consisting of ultrafine powders of titanium, carbon and aluminium as moderator in the form of pellets and the introduction of this alloy into the aluminium melt [51, 52]. TiC is formed as a result of a chain of chemical reactions at the place of introduction of the master alloy, which acts as a reinforcing phase [52–54].

The molten metal matrix solidifies after mixing, securely fixing the reinforcing particles within it. In this case, depending on the purpose of the composite material, it is possible to form a shaped casting or an ingot.

6. CONCLUSIONS

Cast composite materials based on aluminium, magnesium and their alloys provide a level of properties much higher than that of base metals and alloys. This makes CCM promising materials for various branches of engineering.

During obtaining CCM, such parameters of technology are important:

- the choice of the type of matrix alloy;
- the method of its preparation;
- type, size, shape and amount of reinforcing particles;
- the principle and parameters of the introduction of dispersed particles into the melt.

Only the optimal combination of all these elements can provide composite materials with a high level of physical, mechanical and operational properties.

ACKNOWLEDGMENT

This study was supported by the International Visegrad Fund (IVF contract No. 52010054).

REFERENCES

[1] Mavhungu S.T., Akinlabi E.T., Onitiri, M.A. & Varachia F.M. (2017). Aluminum matrix composites for industrial use: advances and trends. *Procedia Manufacturing*, 7, 178–182. Doi: https://doi.org/10.1016/j.promfg.2016.12.045.

[2] Sharma A.K., Bhandari R., Aherwar A., Rimašauskienė R. & Pinca-Bretotean C. (2020). A study of advancement in application opportunities of aluminum metal matrix composites. *Materials Today: Proceedings*, 26, 2419–2424. Doi: https://doi.org/10.1016/j.matpr.2020.02.516.

[3] Kalisz D. & Arustmian A. (2020). Multimetal Stahl 1018 Composite – Structure and Strength Properties. *Archives of Foundry Engineering*, 11/4, 77–82. Doi: https://doi.org/10.24425/afe.2020.133351.

[4] Rohatgi P. (1991). Cast aluminum-matrix composites for automotive applications. *JOM Journal of the Minerals, Metals and Materials Society*, 43(4), 10–15.

[5] Sharma A.K., Bhandari R., Aherwar A. & Pinca-Bretotean C. (2020). A study of fabrication methods of aluminum based composites focused on stir casting process. *Materials Today: Proceedings*, 27, 1608–1612. Doi: https://doi.org/10.1016/j.matpr.2020.03.316.

[6] Lelito J., Żak P.L., Gracz B., Szucki M., Kalisz D., Malinowski P., Suchy J.S. & Krajewski W.K. (2015). Determination of substrate log-normal distribution in the AZ91/SICP composite. *Metalurgija*, 54(1), 204–206.

[7] Saleh B., Jiang J., Fathi R., Xu Q., Wang L. & Ma A. (2020). Study of the microstructure and mechanical characteristics of AZ91-SiC_p composites fabricated by stir casting. *Archives of Civil and Mechanical Engineering*, 20, 1–14. Doi: https://doi.org/10.1007/s43452-020-00071-9.

[8] Chernyshova T.A., Kobeleva L.I. & Bolotova L.K. (2001). Diskretno armirovannyye kompozitsionnyye materialy s matritsami iz alyuminiyevykh splavov i ikh tribologicheskiye svoystva. *Metally*, 6, 85–98 [Чернышова Т.А., Кобелева Л.И. & Болотова Л.К. (2001). Дискретно армированные композиционные материалы с матрицами из алюминиевых сплавов и их трибологические свойства. *Металлы*, 6, 85–98].

[9] Boczkowska A. & Krzesiński G. (2016). *Kompozyty i techniki ich wytwarzania.* Warszawa: Oficyna Wydawnicza Politechniki Warszawskiej.

[10] Boczkowska A., Kapuściński J., Lindemann Z., Witemberg-Perzyk D. & Wojciechowski S. (2003). *Kompozyty*. Warszawa: Oficyna Wydawnicza Politechniki Warszawskiej.

[11] Rohatgi P.K., Kumar P.A., Chelliah N.M. & Rajan T.P.D. (2020). Solidification processing of cast metal matrix composites over the last 50 years and opportunities for the future. *JOM Journal of the Minerals, Metals and Materials Society*, 72, 2912–2926. Doi: https://doi.org/10.1007/s11837-020-04253-x.

[12] Morgan P. (2005). *Carbon Fibers and their Composites*. Boca Raton: CRC Press Taylor and Francis Group.

[13] Matthews F.L. & Rawlings R.D. (1999). *Composite Materials: Engineering and Science*. Sawston: Woodhead Publishing. Doi: https://doi.org/10.1016/C2013-0-17714-8.

[14] Żak P. L., Kalisz D. & Rączkowski G. (2017). Numerical Model of SiC Particle Interaction with Solidification Front in AZ91/(SiC_p) Composite. *Archives of Metallurgy and Materials*, 62 (3), 1625–1628. Doi: https://doi.org/10.1515/amm-2017-0248.

[15] Kondratenko A.N. & Golubkova T.A. (2009). Perspektivnyye tekhnologii polucheniya i oblasti primeneniya nanostrukturnykh metallomatrichnykh kompozitov. *Konstruktsii iz kompozitsionnykh materialov*, 1, 24–25 [Кондратенко А.Н. & Голубкова Т.А. (2009). Перспективные технологии получения и области применения наноструктурных металломатричных композитов. *Конструкции из композиционных материалов*, 1, 24–25].

[16] Gul'bin V.N. & Kolpakov N.S. (2014). Oblegchennyye radiatsionnozashchitnyye kompozity. *Naukoyemkiye tekhnologii*, 3 (15), 4–16 [Гульбин В.Н. & Колпаков Н.С. (2014). Облегченные радиационно-защитные композиты. *Наукоемкие технологии*, 3 (15), 4–16].

[17] Kaczmar J.W., Pietrzak K. & Włosiński W. (2000). The production and application of metal matrix composite materials. *Journal of materials processing technology*, 106(1–3), 58–67. Doi: https://doi.org/10.1016/S0924-0136(00)00639-7.

[18] Bhoi N.K., Singh H. & Pratap S. (2019). Developments in the aluminum metal matrix composites reinforced by micro/nano particles – A review. *Journal of Composite Materials*, 54, 813–833. Doi: https://doi.org/10.1177/0021998319865307.

[19] Maziarz W., Wójcik A., Bobrowski P., Bigos A., Szymański Ł., Kurtyka P., Rylko N. & Olejnik E. (2019). SEM and TEM studies on in-situ cast Al-TiC composites. *Materials Transactions*, 60(5), 714–717. Doi: https://doi.org/10.2320/matertrans.MC201806.

[20] Luong D.D., Gupta N., Daoud A. & Rohatgi P.K. (2011). High strain rate compressive characterization of aluminum alloy/fly ash cenosphere composites. *JOM Journal of the Minerals, Metals and Materials Society*, 63(2), 53–56. Doi: https://doi.org/10.1007/s11837-011-0029-y.

[21] Omrani E., Moghadam A.D., Algazzar M., Menezes P.L. & Rohatgi P.K. (2016). Effect of graphite particles on improving tribological properties Al-16Si-5Ni-5Graphite self-lubricating composite under fully flooded and starved lubrication conditions for transportation applications. *The International Journal of Advanced Manufacturing Technology*, 87(1), 929–939. Doi: https://doi.org/10.1007/s00170-016-8531-6.

[22] Pechnikov A.A., Toleshuly A. & Meshcheryakov Ye.G. (2014). Lityye kompozitsionnyye izdeliya s alyuminiyevoy matritsey. *Izvestiya MGTU "MAMI"*, 1(19/2), 42–44 [Печников А.А., Толешулы А. & Мещеряков Е.Г. (2014). Литые композиционные изделия с алюминиевой матрицей. *Известия МГТУ "МАМИ"*, 1 (19/2), 42–44].

[23] Narayan R. & Rohatgi P.K. (1981). Damping capacity, resistivity, thermal expansion and machinability of aluminium alloy-mica composites. *Journal of Materials Science*, 16(11), 3025–3032.
[24] Baradeswaran A. & Perumal A.E. (2013). Influence of B_4C on the tribological and mechanical properties of Al 7075–B_4C composites. *Composites Part B: Engineering*, 54, 146–152. Doi: https://doi.org/10.1016/j.compositesb.2013.05.012.
[25] Bhushan R.K., Kumar S. & Das S. (2013). Fabrication and characterization of 7075 Al alloy reinforced with SiC particulates. *The International Journal of Advanced Manufacturing Technology*, 65(5–8), 611–624. Doi: https://doi.org/10.1007/s00170-012--4200-6.
[26] Wojcik A., Olejnik E., Bigos A., Chulist R., Bobrowski P., Kurtyka P., Tarasek A., Rylko N., Szymanski L. & Maziarz W. (2020). Microstructural characterization and mechanical properties of in situ cast nanocomposites Al/TiC type. *Journal of Materials Research and Technology*, 9(6), 12707–12715. Doi: https://doi.org/10.1016/j.jmrt.2020.09.012.
[27] Ye T., Xu Y. & Ren J. (2019). Effects of SiC particle size on mechanical properties of SiC particle reinforced aluminum metal matrix composite. *Materials Science and Engineering: A*, 753, 146–155. Doi: https://doi.org/10.1016/j.msea.2019.03.037.
[28] Venkateshwar Reddy P., Suresh Kumar G., Satish Kumar V. & Veerabhadra Reddy B. (2020). Effect of Substituting SiC in Varying Proportions for TiC in Al-5052/TiC/SiC Hybrid MMC. *Journal of Bio- and Tribo-Corrosion*, 6(1), 1–11. Doi: https://doi.org/10.1007/s40735-019-0320-y.
[29] Ferguson J.B., Aguirre I., Lopez H., Schultz B.F., Cho K. & Rohatgi P.K. (2014). Tensile properties of reactive stir-mixed and squeeze cast Al/CuO_{np}-based metal matrix nanocomposites. *Materials Science and Engineering: A*, 611, 326–332. Doi: https://doi.org/10.1016/j.msea.2014.06.008.
[30] Rohatgi P.K., Menezes P.L., Mazzei T. & Lovell M.R. (2011). Tribological Behavior of Aluminum Micro- and Nano-Composites. *International Journal of Aerospace Innovations*, 3(3), 153–162.
[31] Reddy M.P., Shakoor R.A., Parande G., Manakari V., Ubaid F., Mohamed A.M.A. & Gupta M. (2017). Enhanced performance of nano-sized SiC reinforced Al metal matrix nanocomposites synthesized through microwave sintering and hot extrusion techniques. *Progress in Natural Science: Materials International*, 27(5), 606–614. Doi: https://doi.org/10.1016/j.pnsc.2017.08.015.
[32] Amouri K., Kazemi S., Momeni A. & Kazazi M. (2016). Microstructure and mechanical properties of Al-nano/micro SiC composites produced by stir casting technique. *Materials Science and Engineering: A*, 674, 569–578. Doi: https://doi.org/10.1016/j.msea.2016.08.027.
[33] Huang S. & Abbas A. (2020). Effects of tungsten disulfide on microstructure and mechanical properties of AZ91 magnesium alloy manufactured by stir casting. *Journal of Alloys and Compounds,* 817, 153321. Doi: https://doi.org/10.1016/j.jallcom.2019.153321.
[34] Mohammadi H., Emamy M. & Hamnabard Z. (2020). The statistical analysis of tensile and compression properties of the as-cast AZ91-X% B_4C composites. *International Journal of Metalcasting,* 14 (2), 505–517. Doi: https://doi.org/10.1007/s40962-019-00377-2.
[35] Tang X. & Dolman K.F. (2014). Patent No. 2934084. Quebec, Canadian Intellectual Property Office.
[36] Chernysheva T.A., Kurganova Yu.A., Kobeleva L.I., Bolotova L.K., Kalashnikov I.Ye. & Katin I.V. (2007). Kompozitsionnyye materialy s matritsey iz alyuminiyevykh splavov, uprochnennykh chastitsami, dlya par treniya skol'zheniya. *Pokrytiya i materialy spetsial'nogo naznacheniya*, 3, 38–49 [Чернышева Т.А., Курганова Ю.А., Кобелева Л.И., Болотова Л.К., Калашников И.Е. & Катин И.В. (2007). Композиционные материалы с матрицей из алюминиевых сплавов, упрочненных частицами, для пар трения скольжения. *Покрытия и материалы специального назначения*, 3, 38–49].
[37] Vasil'yev V.V. (1990). *Kompozitsionnyye materialy. Spravochnik.* Moskva: Mashinostroyeniye [Васильев В.В. (1990). *Композиционные материалы. Справочник*. Москва: Машиностроение].
[38] DeJack M. (2015). Literature Review of CGI and Ductile Iron and Development of Improved Models for HCF. *Conference: International FEMFAT User Meeting: June 10–12. Steyr.* (pp. 1–48). Steyr: Engineering Center Steyr.
[39] Pikunov M.V. (2005). Plavka metallov. Kristallizatsiya splavov. Zatverdevaniye otlivok. Moskva: MISiS. [Пикунов М.В. (2005). *Плавка металлов. Кристаллизация сплавов. Затвердевание отливок*. Москва: МИСиС].
[40] Yigezu B.S., Mahapatra M.M. & Jha P.K. (2013). Influence of reinforcement type on microstructure, hardness, and tensile properties of an aluminum alloy metal matrix composite. *Journal of Minerals and Materials Characterization and Engineering*, 1(4), 124–130. Doi: https://doi.org/10.4236/jmmce.2013.14022.
[41] Kumar A., Singh R. C. & Chaudhary R. (2020). Recent progress in production of metal matrix composites by stir casting process: An overview. *Materials Today: Proceedings*, 21, 1453–1457. Doi: https://doi.org/10.1016/j.matpr.2019.10.079.
[42] Singh J. & Chauhan A. (2019). A review of microstructure, mechanical properties and wear behavior of hybrid aluminium matrix composites fabricated via stir casting route. *Sādhanā*, 44(1), 16. Doi: https://doi.org/10.1007/s12046-018-1025-5.
[43] Miracle D.B. (2005). Metal matrix composites – From science to technological significance. *Composites science and technology*, 65(15–16), 2526–2540. Doi: https://doi.org/10.1016/j.compscitech.2005.05.027.
[44] Soltani S., Khosroshahi R.A., Mousavian R.T., Jiang Z.-Y., Boostani A.F. & Brabazon D. (2017). Stir casting process for manufacture of Al-SiC composites. *Rare Metals*, 36(7), 581–590. Doi: https://doi.org/10.1007/s12598-015-0565-7.
[45] Nebozhak I.A. (2016). Vliyanye armirovaniya dispersnym intermetallidom FeCr, implantirovannym v gazifitsiruyemuyu model', na strukturu i mekhanicheskiye svoystva splava AK12. *Lit'ye. Metallurgiya. 2016: Materialy XII Mezhdunarodnoy nauchno-prakticheskoy konferentsii: 24–26 maya. Zaporozh'ye*. Zaporozh'ye: ZTPP, 176–178 [Небожак И.А. (2016). Влияние армирования дисперсным интерметаллидом FeCr, имплантированным в газифицируемую модель, на структуру и механические свойства сплава АК12. *Литье. Металлургия. 2016: Материалы XII Международной научно-практической конференции: 24–26 мая. Запорожье*. Запорожье: ЗТПП, 176–178].
[46] Dan O. & Trofimova L. (2021). A Study of the Properties of Forming Mixtures Containing Polystyrene Wastes. *Journal of Casting & Materials Engineering*, 5(2), 14–19. Doi: https://doi.org/10.7494/jcme.2021.5.2.14.
[47] Gusev S.S., Lobkov D.N. & Kazachkov S.S. (1999). Ispol'zovaniye metodov tsentrobezhnogo lit'ya dlya polucheniya izdeliy iz kompozitsionnykh materialov s uprochnennoy poverhnost'yu. *Materialovedeniye*, 5, 50–53 [Гусев С.С., Лобков Д.Н. & Казачков С.С. (1999). Использование методов центробежного литья для получения изделий из композиционных материалов с упрочненной поверхностью. *Материаловедение*, 5, 50–53].
[48] Kevorkijan V. (2003). Functionally graded aluminum-matrix composites. *American Ceramic Society Bulletin*, 82(2), 60–64.
[49] Alekseeva Yu.S. (2008). Primeneniye metoda tsentrobezhnogo lit'ya dlya izgotovleniya vtulok iz gradientnykh kompozitsionnykh materialov. *Vestnik FGOU MGAU*, 4, 96–99 [Алексеева Ю.С. (2008). Применение метода центробежного литья для изготовления втулок из градиентных композиционных материалов. *Вестник ФГОУ МГАУ*, 4, 96–99].
[50] Nukami T. & Flemings M.C. (1995). In situ synthesis of TiC particulate-reinforced aluminum matrix composites. *Metallurgical and Materials Transactions A*, 26(7), 1877–1884.
[51] Olejnik E., Kurtyka P., Tokarski T., Maziarz W., Grabowska B. & Czapla P. (2016). Locally reinforcement TiC-Fe type produced in situ in castings. *Archives of Foundry Engineering*, 16(3), 77–82. Doi: https://doi.org/10.1515/afe-2016-0054.
[52] Maziarz W., Bobrowski P., Wójcik A., Bigos A., Szymański Ł., Kurtyka P., Rylko N. & Olejnik E. (2020). Microstructure and Mechanical Properties of In Situ Cast Aluminum Based Composites Reinforced with TiC Nano-Particles. *Materials Science Forum*, 985, 211–217. Doi: https://doi.org/10.4028/www.scientific.net/MSF.985.211.
[53] Kattner U.R., Lin J.C. & Chang Y.A. (1992). Thermodynamic assessment and calculation of the Ti-Al system. *Metallurgical Transactions A*, 23(8), 2081–2090.
[54] Kalisz D., Żak P.L. & Dan O. (2021). Modeling the Filler Phase Interaction with Solidification Front in Al(TiC) Composite Produced by the In Situ Method. *Materials*, 14(24), 7560. Doi: https://doi.org/10.3390/ma14247560.

Journal of Casting & Materials Engineering Vol. 6 No. 1 (2022) 14–21
https://doi.org/10.7494/jcme.2022.6.1.14

Structural and Morphological Evaluations of Natural Hydroxyapatite from Calcined Animal Bones for Biomedical Applications

Olusola Emmanuel Ojo[a,b*], Olatunde Israel Sekunowo[a], Margaret Okonawan Ilomuanya[c], Oluwashina Philips Gbenebor[a], Samson Oluropo Adeosun[a]

[a]University of Lagos, Faculty of Engineering, Department of Metallurgical & Materials Engineering, Akoka, Lagos, Nigeria
[b]Federal Institute of Industrial Research, Projects Development and Design Department, Cappa Bus Stop, Oshodi, Lagos, Nigeria
[c]University of Lagos, Faculty of Pharmacy, Department of Pharmaceutics and Pharmaceutical Technology, Idi– Araba, Lagos, Nigeria
e-mail: isolyet@yahoo.com

Received: 28 October 2021/Accepted: 17 January 2022 Published online: 8 February 2022
This article is published with open access at AGH University of Science and Technology Press.

Abstract

Several biomedical materials have been employed as drug delivery systems, but natural Hydroxyapatite (HAP) has been proven to be exceptionally better than other materials owing to its excellent bioactivity and biocompatibility properties. In this study, natural HAP was obtained from bovine and caprine bones and comparatively analysed for biomedical applications. The bones were hydrothermally treated, calcined in the temperature range of 700–1100°C, held for 2 hours in an electric furnace to remove the organic contents; milled, sifted with 150 µm mesh sieve and then characterized. It was revealed by Energy Dispersive X-Ray Spectroscopy (EDS) that the bovine and caprine bone samples calcined at 1000°C had calcium/phosphorus ratio (Ca/P) of 1.66 closest to the standard of 1.67. The bovine HAP showed the best crystallinity (86.23%) at 1000°C while caprine HAP had its highest (87.25%) at 1100°C. Fourier Transform Infrared Spectroscopy (FTIR) results revealed that the calcination temperature must be greater than 700°C to isolate high quality HAP. The Scanning Electron Microscopy (SEM) showed that the samples calcined at 800°C had the largest average particle size (85.34 µm) while porosity increases with calcination temperature in both samples. The HAP obtained at a calcination temperature of 1000°C proved to have the best quality for biomedical applications.

Keywords:

hydroxyapatite, calcination, animal bones, crystallinity, porosity

1. INTRODUCTION

The animal bone comprises 65–70% inorganic components and 30–35% organic at the molecular level [1]. Collagen (95%) is the main component of the organic part of the bone with proteins [2]. There are other organic substances like chondroitin sulphate and keratin sulphate with different lipids like phospholipids, fatty acids and cholesterol [3] in minute quantities. The inorganic part of the bone is mainly hydroxyapatite (HAP) $Ca_{10}(PO_4)_6(OH)_2$, which belongs to the group of calcium/phosphate-based biomaterial of ceramic origin with considerable chemical similarity to the inorganic constituent of the bone matrix [4]. Generally, apatite is described by means of the chemical formula $M_{10}(XO_4)_6Z_2$ where M could be Ca^{2+}, Mg^{2+}, Na^{+}, Zn^{2+}, Sr^{2+}, Ba^{2}+, Pb^{2+}or Si^{2+}; X could be P^{5+}, Cr^{5+}, V^{5+} or Mn^{5+} and Z could be Cl^{-}, F^{-} or OH^{-} [5]. HAP is a non-toxic, biocompatible, non-inflammatory and non-immunogenic agent. It is also bioactive because it has the ability to form a bond with the surrounding bone tissue after implantation. Many studies have been carried out on it owing to its chemical and structural similarity to bone minerals [6, 7]. As a result of these properties, it is considered to play a vital role in both medical and nonmedical fields such as drug delivery, orthopedics, dentistry, maxillofacial, skull defects, wound tissue engineering, artificial bone synthesis, biosensor, the removal of heavy metals, and the removal of nitrate from water [8, 9]. HAP can be derived from either a natural source like marine sources (fish bone and fish scale), shell sources (seashell and eggshell) and mineral sources (limestone) [10] or by synthetic methods like sol-gel, wet chemical precipitation, hydrothermal method, microwave irradiation [11–14] etc. Comparatively, natural apatite existing in bones has better biological properties than synthesized HAP. In this regard, researchers have endeavored to isolate HAP scaffolds from natural sources [15] because of the presence of beneficial cations such as Na^{+}, K^{+}, Zn^{2+}, Si^{4+}, Mg^{2+}, Ba^{2+} and anions such

as F^-, CO_3^{2-} etc., which are considered to play important roles in tissue engineering and other biochemical reactions [16]. The trace elements are actively involved in the natural bone metabolism process, while the carbonate ions considered as an impurity in natural HAP help to enhance the mechanical strength, bioactivity and bio-resorbability of the implants. This makes natural HAP highly beneficial and more suitable in some applications (like drug delivery) than synthetic HAP [17, 18]. In this study, caprine and bovine bones were calcined to isolate their HAP and then comparatively analyzed for compositions and physico-chemical properties in relation to biomedical applications. Ojo *et al*. [19] have claimed that, despite their availability, the use of caprine bones has been understudied.

2. MATERIALS AND METHODS

2.1. Preparation of bovine and caprine bone particles

The femur bones of bovine (*Bos Taurus*) and caprine (*Capra aegagrus hircus*) used in this research work were acquired from the Magboro main market in Ogun State, Nigeria. The bovine bones were obtained from ~36 months old and caprine bones from 30–36 months old animals. The dirt and blood on the bone surfaces were washed off thoroughly and then soaked for 96 hours in water to break the firmly adhering tissues, meat, and other impurities on the surface. The bones were broken into 4–10 cm lengths and the marrow were removed. Defatting of the bones was done to remove the proteins and fatty substances in a 10-litre Quink® pressure pot with 4 L of preheated water poured and heated to 120°C for 1.5 hours. On cooling, the bones were then oven dried for 8 hours at 80°C. After drying, calcination was done to remove the organic matter (collagen) present in the bone samples. The bovine and caprine bones were placed into a laboratory furnace (Carbonite, England) with 16,000 cm^3 heating chamber at 10°C/min heating rate for calcination at 700, 800, 900, 1000 and 1100°C; soaked for 2 hours and left overnight to cool to ambient temperature in the furnace. Each of the calcinations was started at the minimum temperature possible in the heating chamber at the beginning of each day. The calcined bone samples were subjected to hammer milling using Broyeur Clero® (Model 13634, 1.5 kV, France). This process facilitated bone size reduction to less than 10mm. Then the bone particles were ball milled using a Faure®machine (Model 28A20:92, France) with 5 kg-ceramic milling balls of 10–20 mm diameter in a 10-litre milling barrel. Ball milling was done at the speed of 40 rpm for 20 hours and then sifted with 150 μm mesh sieve before characterization.

2.2. Physicochemical and morphological characterization

EMPYERN XRD-600 Diffractometer (45 kV, 40 mA) with a CuKα (λ = 1.54 Å) was used to determine the phase composition of the samples. Radiation over the scanning range (2θ) from 5° to 75° and a step size of 0.026°. Using the Equation (1) used by Rana et al. [15], the degree of crystallinity was obtained.

$$X_c(\%) = 1 - \frac{V_{112/300}}{I_{300}} \quad (1)$$

where:

$V_{112/300}$ – intensity of the valley (hollow part) between peaks 112 and 300;
I_{300} – intensity of peak 300.

Similarly, the crystallite size (D) was determined using Scherrer's equation:

$$D = \frac{K\lambda}{\beta\cos\theta} \quad (2)$$

where:

K – constant for spherical crystallite; K = 0.89;
β – full width at half maximum of the peak in radians;
λ – diffraction wavelength (0.154059 nm);
θ – diffraction angle.

The functional groups present in the bovine bone samples (BBS) and caprine bone samples (CBS) were confirmed using Agilent Technologies® (USA) FTIR analyzer in the range of 4000–650 cm^{-1}. The morphology of the BBS and CBS were examined using SEM; model Phenom® Eindhoven, Netherlands. The EDS that was equipped with the SEM was used to analyze the elemental composition of the samples. The chemical composition of the BBS and CBS bone samples were revealed by XRF analyzer while the porosity was determined by analyzing the SEM micrographs 5 times each using Image J® software and the average values were recorded.

3. RESULTS AND DISCUSSION

3.1. General observations

During the calcination process of the bone samples, between 170°C and slightly greater than 700°C, pungent and choking fumes were observed from the furnace exhaust pipe. This is the temperature range at which the organic component decomposed. The pH of the fumes was ~9 when tested with damp litmus paper. Brownish and bluish colour patches were observed on the bone samples, especially the bovine ones calcined at 1100°C. It was also observed that at 800°C, the physicochemical properties of both bone samples were all deviant unlike the properties at other calcination temperature. The calcination was repeated at the temperature (800°C) for confirmation; the same results were obtained. This might indicate that 800°C is a transitional temperature in the calcination process.

3.2. Bone calcination

The HAP was extracted from the bovine and caprine bones by means of the thermal decomposition process. In the process, at highest calcination temperature (1100°C), the largest quantity of organic matter (collagen) was dispelled.

After calcination at this temperature, there was a 40.6% and 45.6% weight reduction, which signifies the quantity of collagen dispelled in BBS and CBS respectively. This was as a result of the enormous heat generated at this temperature (1100°C), which was high enough to rid the bone samples of the inorganic content, in contrast to what happened at 700°C where only 31.2% of the collagen was eliminated from the BBS. The black color of the sample calcined at 700°C revealed the incomplete removal of the organic matrix within the bone. Consequently, calcination at temperature close to 700°C is not beneficial for removing residual organic content for the isolation of pure HAP from the bone samples. As expected, the percentage weight loss is directly proportional to the calcination temperature (Fig. 1).

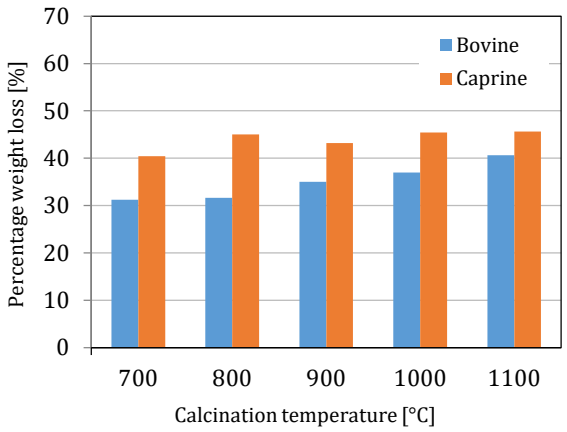

Fig. 1. Percentage weight loss in calcined BBS and CBS at different calcination temperature

3.3. Chemical composition of calcined bone

The XRF analysis results of the calcined and raw BBS and CBS at different calcination temperature are presented in Tables 1 and 2 showing the chemical compositions of these materials in oxide form. Oxides of calcium and phosphorous are the main components in the bone samples with phosphoric pentoxide (P_2O_5) and calcium oxide (CaO) as 31.08 wt.% and 40.36 wt.% in BBS; 30.90 wt.% and 41.96 wt.% in CBS respectively. The loss on ignition (LOI) of raw BBS and CBS were 26.64% and 24.89% respectively. The LOI indicates the removal of the inorganic substance of the bone samples, which is probably the reason for its absence in the calcined samples. The iron III oxide (Fe_2O_3) and copper II oxide (CuO) which are known for their brownish and bluish color respectively could have been concluded to be responsible for the coloration of the samples at calcination temperature of 1100°C, but their quantity in the raw samples were negligible. Magnesium oxide, strontium oxide, silica, and copper oxide were found in very minute quantities in both bone samples.

3.4. Elemental composition of calcined bones

The elemental composition of the raw and calcined BBS and CBS at different calcination temperature were investigated by EDS analysis as shown in Tables 3 and 4.

Table 1
Oxide composition of raw and calcined BBS at different calcination temperature in weight percentage

Oxides	Raw	700°C	800°C	900°C	1000°C	1100°C
CaO	40.36	52.36	25.38	46.79	46.40	46.92
P_2O_5	31.80	40.95	22.07	38.83	45.33	48.91
Fe_2O_3	0.19	0.019	0.52	0.024	0.05	0.02
SiO_2	0.18	0.33	7.70	0.67	1.52	0.68
MgO	0.43	1.65	0.88	0.66	1.22	–
CuO	0.016	–	0.0011	–	0.004	0.0002
SrO	0.15	1.26	0.59	0.81	1.02	0.86
Others	0.234	3.431	42.86	12.22	4.456	2.61
LOI	26.64	–	–	–	–	–

Table 2
Oxide composition of raw and calcined CBS at different calcination temperature in weight percentage

Oxides	Raw	700°C	800°C	900°C	1000°C	1100°C
CaO	41.95	52.61	45.14	50.47	46.44	47.44
P_2O_5	30.90	40.36	38.00	40.94	45.00	51.16
Fe_2O_3	–	0.04	0.22	0.19	0.03	0.13
SiO_2	0.20	0.51	3.81	0.56	1.32	0.89
MgO	0.50	0.64	1.27	0.46	1.16	–
CuO	0.006	–	–	–	0.0003	0.000064
SrO	0.20	2.07	1.24	2.17	1.17	1.13
Others	1.354	3.77	10.32	5.21	4.88	–
LOI	24.89	–	–	–	–	–

Table 3
Elemental composition of calcined BBS at different calcination temperature in weight percentage

Elements	Raw	700°C	800°C	900°C	1000°C	1100°C
Ca	50.44	69.43	55.69	66.24	66.19	63.97
P	16.75	18.33	20.68	18.26	23.08	23.27
Mg	0.66	0.53	2.38	0.70	0.91	1.08
K	0.6	0.62	0.97	1.00	0.53	0.67
Na	0.5	0.58	1.12	0.43	0.75	0.87
C	17.17	1.07	0.89	1.34	1.10	1.36
O	5.99	–	–	–	–	–
Ag	1.86	1.20	1.30	1.89	1.54	1.63
Si	1.55	0.48	4.93	0.65	0.52	0.6
N	1.46	–	0.19	–	0.39	0.28
Al	1.33	0.40	4.16	0.63	0.63	0.73
S	0.72	0.16	0.5	0.36	0.34	0.30

Table 4
Elemental composition of calcined CBS at different calcination temperature in weight percentage

Elements	Raw	700°C	800°C	900°C	1000°C	1100°C
Ca	44.31	66.91	62.96	66.93	65.29	64.73
P	13.8	18.58	21.73	18.48	22.77	23.0
Mg	0.52	0.59	1.96	0.80	0.97	1.12
K	0.33	0.81	0.75	0.99	0.56	0.57
Na	0.26	0.39	0.72	0.56	0.52	0.62
C	30.02	1.18	0.81	1.03	2.30	0.93
O	5.17	–	–	–	–	–
Ag	0.94	1.92	1.82	1.66	1.42	1.56
Si	2.2	0.65	1.38	0.72	0.72	0.49
N	–	–	0.16	–	0.60	0.38
Al	1.70	0.94	1.51	0.81	0.69	0.61
S	0.75	0.38	0.33	0.55	0.31	0.32

Calcium, carbon, phosphorus and oxygen were present in significant amounts in both raw and calcined bone samples while the presence of trace beneficial elements such as sodium, magnesium, potassium and silicon were detected also in the crystal lattice of the isolated HAP. Carbon and oxygen were significantly present in both raw samples, with traces of sulfur, and nitrogen as they were the main constituents of collagen being a protein. Carbon in raw samples reduced from 17.7% to 1.36% and 30.02% to 0.93% at 1100°C in BBS and CBS respectively. Similarly, as the calcination temperature increases, oxygen is driven off from the organic substance [20]. The composition of these elements reduced drastically as the calcination was carried out on both samples. This might not be unconnected with the fact that the calcination process expelled the organic substance; consequently, the elements that make up the organic substance will be reduced in the crystal lattice of the samples after calcination. The sum of the weight percentage of the carbon and oxygen present in raw CBS is more than that of BBS. This is also in accordance with the results in Figure 1, where the percentage weight loss of calcined CBS is more than that of BBS at any calcination temperature, indicating that CBS has a higher percentage of organic substances. The percentage of phosphorus in the raw samples was found to have increased from 16.75% to 23.27% and 13.8% to 23.0% at 1100°C in BBS and CBS respectively while calcium in the raw samples was found to increase from 50.44% to 63.97% and 44.31% to 64.73% at 1100°C in BBS and CBS respectively. This implies that calcium and phosphorus increase together with an increase in calcination temperature because of the other elements (Carbon and oxygen) that were eliminated as the calcination temperature increases. Similar to the work of Venkatesan & Kim [21], the increase does not tend to be directly proportional to the temperature increase.

The Ca/P ratios of calcined BBS and CBS are presented in Figure 2. The Ca/P ratio for the two calcined bone samples from 700 to 1100°C show deviations from the theoretical value for pure stoichiometric HAP of 1.67. In fact, natural HAP is non-stoichiometric (exhibits a Ca/P ratio higher than 1.67) [22]. The Ca/P ratios of HAP derived from both bone samples obtained at 1000°C have the closest values of 1.66.

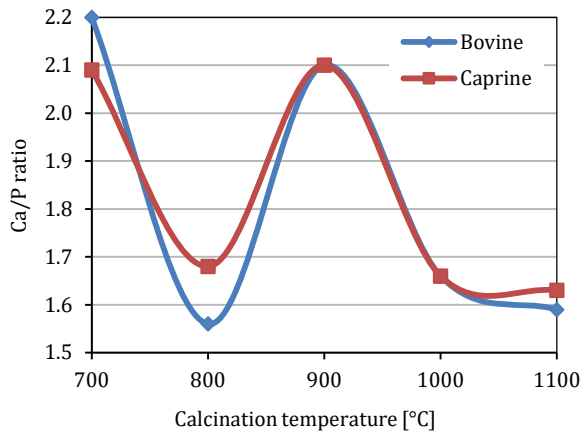

Fig. 2. Calcium-to-Phosphorus ratio of BBS and CBS at different calcination temperature

The range of Ca/P ratio of HAP derived from both samples in the present study appear to be markedly higher at 1.59–2.20 compared to those reported from recent study by Ramesh et al. [18] at 1.58–1.88. Also, the CBS is higher at 1.63–2.09 compared with 1.61–1.79. Researchers have been able to identify the factors that could contribute to the deviation of Ca/P ratio from the theoretical value of 1.67. These are calcination conditions like the holding temperature and atmosphere of the calcination process. These will significantly affect the quantity and type of calcium compounds which would appear in the resultant HAP phase [23]. Moreover, ions such as Ca^{2+}, PO_4^{3-} and OH^- exist in natural tissues and their intensity may vary depending on the nutrition and diet of the animal [24].

3.5. Identification of functional groups in HAP

The FTIR has been extensively used for identification of the characteristic functional groups in HAP. These include phosphate (PO_4^{3-}), hydroxyl (OH^-) and carbonate (CO_3^{2-}). In this study, BBS and CBS, the (CO_3^{2-}) appeared at 872 cm^{-1}, 1409–1424 cm^{-1} and 1446–1484 cm^{-1}, the presence of (OH^-) was shown at 3571 cm^{-1}. The (PO_4^{3-}) was revealed at the 913 cm^{-1}, 1006–1029 cm^{-1}, 1088 cm^{-1} and 2013–2020 cm^{-1}. The FTIR spectra of raw and calcined BBS and CBS at 700–1100°C are shown in Figures 3 and 4.

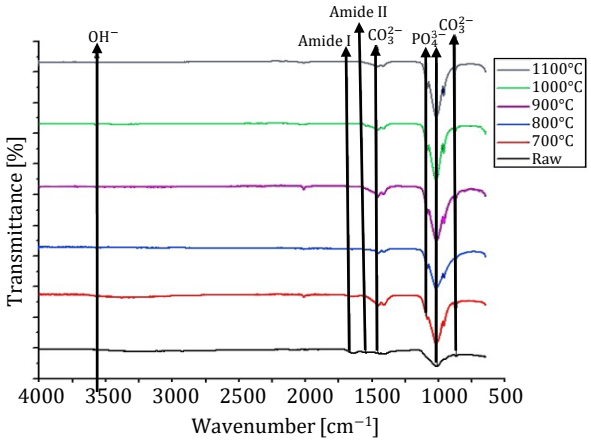

Fig. 3. FTIR spectra of raw and calcined BBS at different calcination temperature

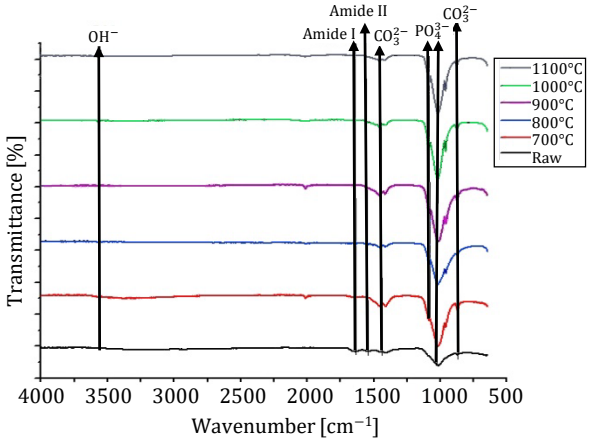

Fig. 4. FTIR spectra of raw and calcined CBS at different calcination temperature

The raw BBS showed characteristic band of amide I and II at 1640 cm^{-1} and 1543 cm^{-1} also for CBS at 1636 cm^{-1} and 1543 cm^{-1} respectively. This is due to the presence of the organic moieties in the raw samples. The HAP obtained from BBS and CBS at 700°C showed all the characteristic bands of the HAP with amide I band, which means the presence of collagen but from calcination temperature of 800–1100°C, all the collagen bands start to disappear. The intensities of both amide bands I and II are lower in the BBS than CBS, which implies that the former has a lower amount of organic phase than the latter. As the calcination temperature increases, the amide I peak gradually reduces until it totally disappeared at 800°C in BBS and 900°C in CBS. Amide II disappeared completely at 700°C in both samples. Moreover, the appearance of an additional peak at 962–958 cm^{-1} and 1088 cm^{-1} due to the symmetrical stretching of phosphate (PO_4^{3-}) in the bones calcined at temperature above 700°C, which was not present in raw BBS and CBS, indicates that the shielded HAP was being freed from organic matter at high temperature. The most intensive and sharpest bands in the range of 1021–1034 cm^{-1} correspond to asymmetric stretching vibrations ($\nu 3$). Its intensity increases with the increase in calcination temperature. Further, the bands between 2080–2013 cm^{-1} due to the overtones and combination of the $\nu 3$ and $\nu 1$ (PO_4^{3-}) were also observed but the intensity of the $\nu 2$ was found to decrease with the increase in the temperature of calcinations. With the increase of the calcination temperature, the relative intensities of the OH^- vibration bands, which did not appear in both raw samples but started appearing at 800–1100°C at band 3571 cm^{-1} for CBS and only from 900–1100°C BBS, show a decrease in intensity in the CBS and thus indicating the process of dehydroxylation, where OH^- is released by the formation of water molecules. The HAP isolated from BBS showed bands between 1461–1446 cm^{-1} and 1420–1409 cm^{-1} and CBS at 1484–1446 cm^{-1} and 1424–1409 cm^{-1} at calcination temperature range of 700–1100°C due to asymmetric stretching or $\nu 3$ of carbonate. The weak band in BBS and CBS at 872–880 cm^{-1} shows out of plane carbonate band, which disappear as the temperature increases [25] and a small band at 667 cm^{-1} for raw CBS, which is associated with the bending vibration of a hydroxyl group of HAP [26]. There was no visible OH^- in both samples at 3571 cm^{-1} before heating but after, which is possibly because of overlapping of impurity bands or masking effect of other impurity bands over it [15]. The absorbed water band (3276 cm^{-1}) appeared in the raw sample and the one calcined at 700°C in BBS and CBS but disappeared with the increase in calcination temperature. It must be noted that the intensities and position of the corresponding absorption bands may be caused by the change in the molecular environment of the HAP [27].

3.6. Crystallographic analysis of calcined HAP

The phase composition analysis of the samples was performed. Figures 5 and 6 show the XRD patterns of raw and calcined BBS and CBS obtained by varying the calcination temperature from 700–1100°C. The XRD parameters of BBS and CBS show identical phases present. The intensities of BBS and CBS dispersed by X-ray radiation were found to be 609 and 573 au respectively, which are relatively low intensities with a wider peak. This is due to the strong presence of organic contents (collagen) in the bone. The amorphous phase disappeared as the calcination temperature increases. It was observed that as the calcination temperature increases, the peak intensity increases with a decrease in the width of the peak, indicating the removal of the organic portion. This also means increasing crystalline nature and crystal size. The CBS in all the calcination temperature was revealed to have lower HAP peak intensities than the BBS. This might not be unconnected with the presence of higher organic content in CBS than that of BBS as revealed during the calcination process. The samples calcined at 700°C in both samples showed wider peak of low intensity, which was a slight improvement over the raw samples, indicating the incomplete removal of organic matter present in the bone matrix. However, thermal calcinations from 800°C showed intense and sharp peaks indicating the crystalline nature and complete removal of organic matter. Blanco et al. [28] revealed that the highest diffraction peak height is related to the amount of crystalline material in the sample. This showed that both raw and calcined CBS have lower crystalline HAP phase when compared with BBS, which indicates more amorphous collagen than the BBS. The XRD patterns of the samples at the range of calcination temperature used in this study do not reveal any other peak apart from HAP's. This is an indication that the HAP derived from the two samples showed thermal stability even at the highest temperature (1100°C) [18].

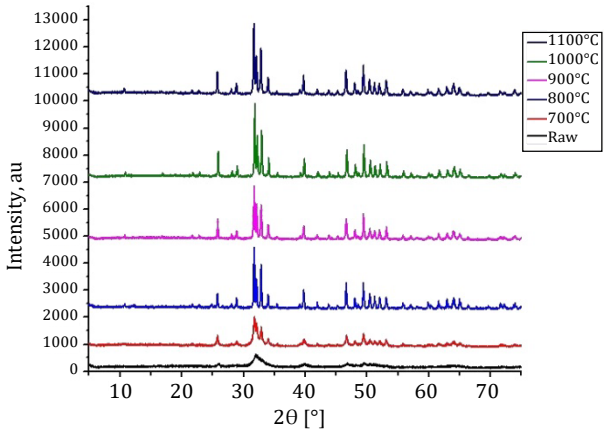

Fig. 5. XRD pattern of raw and calcined BBS at different calcination temperature

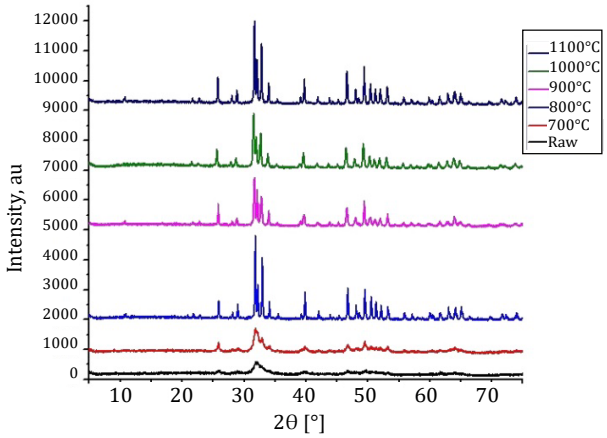

Fig. 6. XRD pattern of raw and calcined CBS at different calcination temperature

Table 5 shows the parameters obtained from XRD spectra; the peak intensity, crystallinity index and crystallite size obtained at the different calcination temperatures. There is no separated peak between 112 and 300. It is important to note that dehydroxylation of the HAP phase would cause a small degree of peak shifting in the XRD trace.

Table 5
Crystallographic parameters of raw and calcined BBS and CBS at different calcination temperature

Temperature	Samples	Intensity peak [au]	Crystallinity index [%]	Crystallite size [nm]
Raw	Bovine	609	No separated peaks	–
	Caprine	573	No separated peaks	–
700°C	Bovine	1201	50.8	39.88
	Caprine	910	24.79	39.89
800°C	Bovine	2410	83.47	53.18
	Caprine	2937	88.17	53.19
900°C	Bovine	2073	84.5	53.18
	Caprine	1729	78.77	45.57
1000°C	Bovine	2871	86.23	53.79
	Caprine	1956	75.31	40.31
1100°C	Bovine	2749	83.4	53.78
	Caprine	2890	87.25	53.78

The degrees of crystalline and crystallite size in both samples tend to increase with an increase in calcination temperature. Zhang et al. [29] revealed that increasing crystallinity of nCaP could slow drug release rate. Also, lower crystallinity exhibited higher drug loading capacity due to presence of more Ca^{2+} adsorption sites on the surface. Similarly, Sanosh et al. [30] reported that the HAP with high crystallinity have little or no activity towards bio-resorption, which is important for the formation of chemical bonding with surrounding hard tissues and fully developed crystalline HAP structure is insoluble in physiological environment expected to be less metabolically active than the crystalline HAP. Additionally, the crystallite size was not consistent with calcination temperature; it was believed that crystal size was closely related to the age of the animal, especially the age of the crystal. The crystal harvested from young postnatal animals was reported to be shorter and thicker than that from mature individual [31].

When crystallinity index (X_c) ≥ 70% usually considered to be a high degree of crystal; 30% < X_c < 70% Medium degree of crystal and when X_c < 30%, it is considered low degree of crystal.

3.7. Calcined HAP morphology and size examination

The scanning electron micrographs and average particle size of the raw and calcined BBS and CBS at 700–1100°C are presented in Table 6 and Figure 7.

Table 6
Average particle size of raw and calcined BBS and CBS at different temperature in micrometer

Samples	Raw	700°C	800°C	900°C	1000°C	1100°C
BBS	52.4	15.52	85.34	12.36	8.35	8.14
CBS	40.7	13.13	88.31	10.01	7.14	7.04

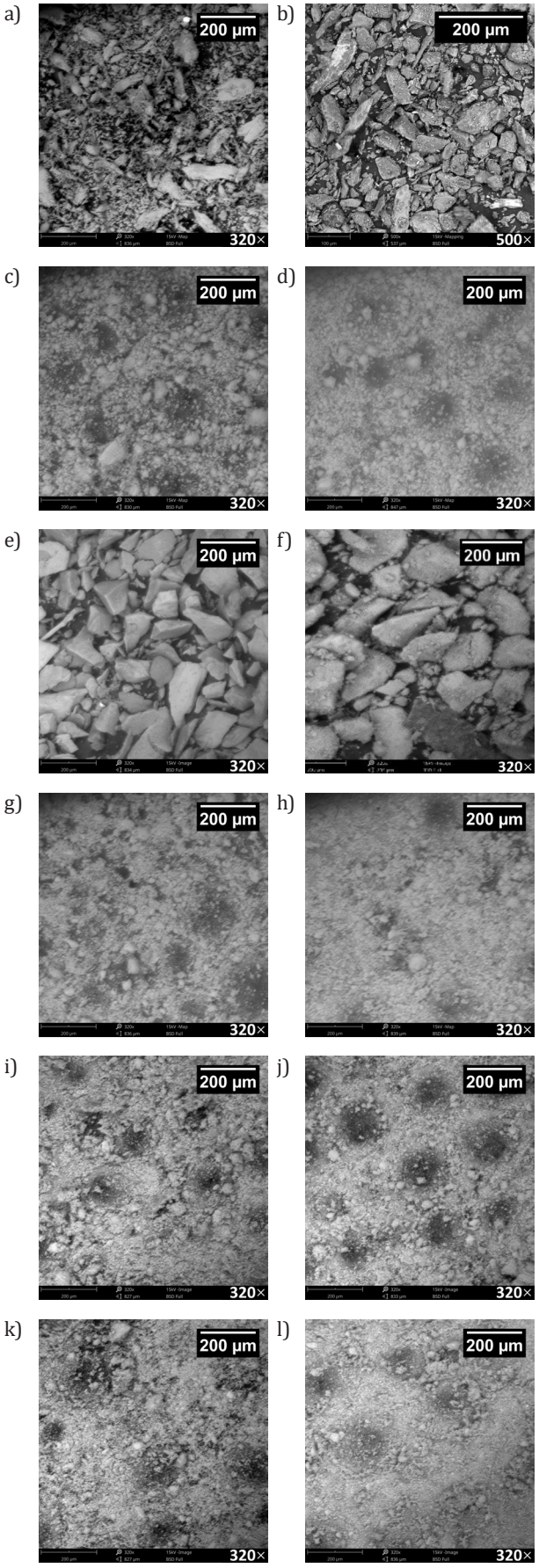

Fig. 7. SEM Morphology of raw and calcined BBS and CBS: a) BBS Raw; b) CBS Raw; c) BBS 700°C; d) CBS 700°C; e) BBS 800°C; f) CBS 800°C; g) BBS 900°C; h) CBS 900°C; i) BBS 1000°C; j) CBS 1000°C; k) BBS 1100°C; l) CBS 1100°C

The morphologies of raw BBS and CBS look like mass of aggregates that have low surface area and show a wide range of particle size and shapes with edges and corners rather than being spherical. This irregularity in size and shape of the particles might be due to the presence of collagen in the raw samples, which means more toughness and subsequently more resistance to milling [19]. In comparison, the calcined bone samples show some alteration in their mophologies and particle size reduction was maximal, exhibiting higher surface area [32]. This might be attributed to less energy requirement for their size reduction as the organic moiety, which served as the matrix had been eliminated by heat generated at high temperature of the calcination process. Calcined samples at 700°C tend to have a larger particles size, more noticeable in BBS. This might be due to the incomplete removal of collagen. The particles become finer as the calcination temperature increases. The particle size, shape and surface roughness have effect on the properties of the particles. The particle size plays an important role in the drug release profile of the particles [33]. Moreover, the morphology of HAP particles also depends on the source of the bone, holding time and temperature of calcination. It might also be influenced by the gender, age, and food habit of the animals from which the bone was collected. Hence, more studies are required to understand the influence of these biological factors on the morphology.

3.8. Porosity analysis of calcined HAP

The porosity of the calcined BBS and CBS at different temperature is shown in Table 7. Porous HAP is an excellent drug carrier. Netz et al. [34] conducted in vitro tests to show that the porosity of HAP greatly influenced drug release kinetics by using HAP with high porosity (82.63%), which exhibited irregular release of cisplatin as high porosity could cause an irregular structure, which may have affected the cisplatin release. The HAP porosity would be useful in the drug delivery systems, only if the porosity is less than 78%. HAP of lower porosity showed significant initial burst release. It was believed that a higher porosity could provide more motion freedom of the molecules to be regularly carried out from the porous structure of HAP. The porosity in the two samples reduces with increase in calcination temperature. This may be attributed to the tighter packing of HAP at a high temperature, due to the improved crystallinity of the structure [35]. Also, the loading efficiency increases with porosity [17].

Table 7
Porosity of raw and calcined BBS and CBS at different temperature in percentage

Samples	Raw	700°C	800°C	900°C	1000°C	1100°C
BBS	43.1	38.7	29.37	34.84	33.56	32.92
CBS	25.6	40.42	24.71	36.32	31.20	28.64

4. CONCLUSIONS

In this research, the best Ca/P ratio of 1.66, which is close to the standard (1.67) was obtained at 1000°C. On average, the BBS HAP had the highest degree of crystallinity (86.23%) at 1000°C while CBS HAP had its (87.25%) at 1100°C. It was also observed that calcination at 700°C gave HAP of the worst quality. The composition, morphology and particle size of samples calcined at 800°C were deviant unlike the properties at other calcination temperature. It might be a transition temperature at which the cohesive forces are broken down in the samples. The calcination affected the quantity of major elements like calcium and phosphorus that increase with temperature. In contrast, other elements like carbon, oxygen, sulfur that are associated with organic moieties reduced drastically at the elevated temperature. The minor elements like sodium, magnesium etc., were still present in the HAP even at the highest temperature (1100°C). The calcined bone samples when compared with raw samples showed some alteration in its morphology with spherical agglomerates in high surface area HAP particles. There was particle size and porosity reduction with increase in calcination temperature in both samples. At 1100°C and 800°C, the smallest and largest particle size respectively were recorded with BBS and CBS having 8.14 μm and 7.04 μm also 85.34 μm and 88.31 μm particle size respectively. Samples calcined at 1100°C had the least porosity. However, a calcination temperature of 1000°C has proven to be the best temperature for the isolation of the best quality HAP from both BBS and CBS.

REFERENCES

[1] Khandelwal H. & Prakash S. (2016). Synthesis and characterization of hydroxyapatite powder by eggshell. *Journal of Minerals and Materials Characterization and Engineering*, 4(2), 119–126. Doi: https://dx.doi.org/10.4236/jmmce.2016.42011.

[2] Venkatesan J., Lowe B., Manivasagan P., Kang K.-H., Chalisserry E.P., Anil S., Kim D.G. & Kim S.-K. (2015). Isolation and characterization of nano-hydroxyapatite from salmon fish bone. *Materials*, 8(8), 5426–5439. Doi: https://doi.org/10.3390/ma8085253.

[3] Bano N., Jikan S.S., Basri H., Adzila S. & Zago D.M. (2019). XRD and FTIR study of A&B type carbonated hydroxyapatite extracted from bovine bone. In: *Proceedings of the AIP Conference*, AIP Publishing, Article ID 020100.

[4] Zhu Y., Murali S., Stoller M.D., Ganesh K.J., Cai W., Ferreira P.J., Pirkle A., Wallace R.M., Cychosz K.A. , Thommes M., Su D., Stach E.A. & Ruoff R.S. (2011). Carbon-based supercapacitors produced by activation of graphene. *Science*, 332(6037), 1537–1541. Doi: https://doi.org/10.1126/science.1200770.

[5] Shalaby S.W. & Salz U. (Eds.) (2007). Polymers for dental and orthopedics applications. *Boca Raton*: CRC Press.

[6] Fahmy M.D., Jazayeri H.E., Razavi M., Masri R. & Tayebi L. (2016). 3-Dimensional bioprinting materials with potential application in preprosthetic surgery. *Journal of Prosthodontics*, 25(4), 310–318. Doi: https://doi.org/10.1111/jopr.12431.

[7] Dhandayuthapani B., Yoshida Y., Maekawa T. & Sakthi Kumar D. (2011). Polymeric scaffolds in tissue engineering application: A review. *International Joutnal of Polymer Science*, Article ID 290602. Doi: https://doi.org/10.1155/2011/290602.

[8] Manalu J.L. Soegijono B. & Indrani D.J. (2015). Characterization of hydroxyapatite derived from bovine bone. *Asian Journal of Applied Sciences*, 3(4), 758–765.

[9] Rajesh R., Hariharasubramanian A. & Ravichandran D. (2012). Chicken bone as a bioresource for the bioceramic (hydroxyapatite). *Phosphorus, Sulfur, and Silicon and the Related Elements*, 187(8), 914–925. Doi: https://doi.org/10.1080/10426507.2011.650806.

[10] Mohd Pu'ad N.A.S., Koshy P., Abdullah H.Z., Idris M.I. & Lee T.C. (2019). Syntheses of hydroxyapatite from natural sources. *Heliyon*, 5(5), e01588. Doi: https://doi.org/10.1016/j.heliyon.2019.e01588.

[11] Agrawal K., Singh G., Puri D. & Prakash S. (2011). Synthesis and characterization of hydroxyapatite powder by Sol-Gel method for biomedical application. *Journal of Minerals and Materials Characterization and Engineering*, 10(8), 727–734. Doi: https://doi.org/10.4236/jmmce.2011.108057.

[12] Gentile P., Wilcock C.J., Miller C.A., Moorehead R. & Hatton P.V. (2015). Process optimisation to control the physico-chemical characteristics of biomimetic nanoscale hydroxyapatites prepared using wet chemical precipitation. *Materials*, 8(5), 2297–2310. Doi: https://doi.org/10.3390/ma8052297.

[13] Yang Y., Wu Q., Wang M., Long J. & Mao Z. (2014). Hydrothermal synthesis of hydroxyapatite with different morphologies: Influence of supersaturation of the reaction system. *Crystal Growth and Design*, 14(9), 4864–4871. Doi: https://doi.org/10.1021/cg501063j.

[14] Kumar G.S., Sathish L., Raji G. & Girijab E.K. (2015). Utilization of snail shells to synthesize hydroxyapatite nanorods for orthopedic applications. *RSC Advances*, 5(49), 39544–39548. Doi: https://doi.org/10.1039/C5RA04402B.

[15] Rana M., Akhtar N., Rahman S., Jamil H. & Asaduzzaman S.M. (2017). Extraction of hydroxyapatite from bovine and human cortical bone by thermal decomposition and effect of gamma radiation: A comparative study. *International Journal of Complementary & Alternative Medicine*, 8(3), 00263. Doi: https://doi.org/10.15406/ijcam.2017.08.00263.

[16] Akram M., Ahmed R., Shakir I., Ibrahim W.A.W. & Rafaqat H. (2014). Extracting hydroxyapatite and its precursors from natural resources. *Journal of Materials Science*, 49(4), 1461–1475. Doi: https://doi.org/10.1007%2Fs10853-013-7864-x.

[17] Murugan R. & Ramakrishna S. (2005). Porous bovine hydroxyapatite for drug delivery. *Journal of Applied Biomaterials & Biomechanics*, 3(2), 93–97.

[18] Ramesh S., Looa Z.Z., Tana C.Y., Chewb W.J.K., Chinga Y.C., Tarlochanc F., Chandrand H., Krishnasamye S., Bangf L.T. & Sarhan A.A.D. (2018). Characterization of biogenic hydroxyapatite derived from animal bones for biomedical applications. *Ceramics International*, 44(9), 10525–10530. Doi: https://doi.org/10.1016/j.ceramint.2018.03.072.

[19] Ojo O.E., Sekunowo I.O., Ilomuanya M.O., Gbenebor P.O. & Adeosun S.O. (2021). Compositions and thermo-chemical analysis of bovine and caprine bones. *Kufa Journal of Engineering*, 12(3), 56–68. Doi: https://doi.org/10.30572/018/kje/120305.

[20] Ofudje E.A., Rajendran A., Adeogun A.I., Idowu M.A., Kareem S.O. & Pattanayak D.K. (2017). Synthesis of organic derived hydroxyapatite scaffold from pig bone waste for tissue engineering applications. *Advanced Powder Technology*, 29(1), 1–8. Doi: https://doi.org/10.1016/j.apt.2017.09.008.

[21] Venkatesan J. & Kim S.K. (2010). Effect of temperature on isolation and characterization of hydroxyapatite from tuna *(Thunnus obesus)* bone. *Materials*, 3(10), 4761–4772. Doi: https://doi.org/10.3390/ma3104761.

[22] Figueiredo M., Fernando A., Martins G., Freitas J., Judas F. & Figueiredo H. (2010). Effect of the calcination temperature on the composition and microstructure of hydroxyapatite derived from human and animal bone. *Ceramics International*, 36(8), 2383–2393. Doi: https://doi.org/10.1016/j.ceramint.2010.07.016.

[23] Ooi C.Y., Hamdi M. & Ramesh S. (2007). Properties of hydroxyapatite produced by annealing of bovine bone. *Ceramics International*, 33(7), 1171–1177. Doi: https://doi.org/10.1016/j.ceramint.2006.04.001.

[24] Sofronia A.M., Baies R., Anghel E.M., Marinescu C.A. & Tanasescu S. (2014). Thermal and structural characterization of synthetic and natural nanocrystalline hydroxyapatite. *Materials Science and Engineering: C*, 43, 153–163. Doi: https://doi.org/10.1016/j.msec.2014.07.023.

[25] Nga N.K., Giang L.T., Huy T.Q., Viet P.H. & Migliaresi C. (2014). Surfactant-assisted size control of hydroxyapatite nanorods for bone tissue engineering. *Colloids and Surfaces B: Biointerfaces*, 116, 666–673. Doi: https://doi.org/10.1016/j.colsurfb.2013.11.001.

[26] Shavandi A., Bekhit A.E., Ali A. & Sun Z. (2015). Synthesis of nano-hydroxyapatite (nHA) from waste mussel shells using a rapid microwave method. *Materials Chemistry and Physics*, 149–150, 607–616. Doi: https://doi.org/10.1016/j.matchemphys.2014.11.016.

[27] Bahrololoom M.E., Javidi M., Javadpour S. & Ma J. (2009). Characterisation of natural hydroxyapatite extracted from bovine cortical bone ash. *Journal of Ceramic Processing Research*, 10(2), 129–138. Doi: https://doi.org/10.36410/jcpr.2009.10.2.129.

[28] Blanco A., Monte M.C., Campano C., Balea A., Merayo N. & Negro C. (2018). Nanocellulose for industrial use: cellulose nanofibers (CNF), cellulose nanocrystals (CNC), and bacterial cellulose (BC). In: C.M. Hussain, Handbook of Nanomaterials for Industrial Applications *Elsevier,* 74–126. Doi: https://doi.org/10.1016/B978-0-12-813351-4.00005-5.

[29] Zhang H., Yan D., Gedara S.M.K., Marakkalage S.S.F.D., Methlal J.G.K, Han Y.Ch. & Dai H.L. (2017). View effects of crystallinity and surface modification of calcium phosphate nanoparticles on the loading and release of tetracycline hydro-chloride. *IOP Conference Series: Materials Science and Engineering*, 182, 012052. Doi: https://doi.org/10.1088/1757-899X/182/1/012052.

[30] Sanosh K.P., Chu M.-C., Balakrishnan A., Kim T.N. & Cho S.-J. (2009). Preparation and characterization of nano-hydroxyapatite powder using sol-gel technique. *Bulletin of Materials Science*, 32(5), 465–470.

[31] Liu Q., Huang S., Matinlinna J.P., Chen Z. & Pan H. (2013). Insight into biological apatite: physiochemical properties and preparation approaches. *BioMed Research International*. Doi: https://doi.org/10.1155/2013/929748.

[32] Nisar J., Razaq R., Farooq M., Iqbal M., Khan R.A., Sayed M., Shah A. & Rahman I. (2017). Enhanced biodiesel production from *Jatropha* oil using calcined waste animal bones as catalyst. *Renewable Energy,* 101, 111–119. Doi: https://doi.org/10.1016/j.renene.2016.08.048.

[33] Sasikumar S. (2013.) Effect of particle size of calcium phosphate based bioceramic drug delivery carrier on the release kinetics of ciprooxacin hydrochloride: An *in- vitro* study. *Frontiers of Materials Science in China*, 7(3), 261–268. Doi: https://doi.org/10.1007/s11706-013-0216-6.

[34] Netz D.J.A., Sepulveda P., Pandolfelli V.C., Spadaro A.C.C., Alencastre J.B., Lopes Badra Bentley M.V. & Marchetti J.M. (2001). Potential use of gelcasting hydroxyapatite porous ceramic as an implantable drug delivery system. *International Journal of Pharmaceutics*,, 213(1–2), 117–125. Doi: https://doi.org/10.1016/S0378-5173(00)00659-1.

[35] Mohammad N.F., Othman R. & Yeoh F.-Y. (2014). Nanoporous hydroxyapatite preparation methods for drug delivery applications. *Reviews on Advanced Materials Science*, 38, 138–147.

Journal of Casting & Materials Engineering Vol. 6 No. 1 (2022) 22–32
https://doi.org/10.7494/jcme.2022.6.1.22

Strength, Water Absorption, Thermal and Antimicrobial Properties of a Biopolymer Composite Wound Dressing

Chiosa Cletus Odili[a*], Olatunde Israel Sekunowo[a], Margaret Okonawan Ilomuanya[b], Oluwashina Philips Gbenebor[a], Samson Oluropo Adeosun[a, c]

[a] University of Lagos, Faculty of Engineering, Department of Metallurgical and Materials Engineering, Nigeria
[b]University of Lagos, Faculty of Pharmacy, Department of Pharmaceutics and Pharmaceutical Technology, Nigeria
[c]Durban University of Technology, Durban South Africa, Industrial Engineering Department
**e-mail:* chiosa.odili@gmail.com

Received: 15 May 2021/Accepted: 8 February 2022/ Published online: 8 March 2022
This article is published with open access at AGH University of Science and Technology Press.

Abstract

Conventional wound material allows bacterial invasions, trauma and discomfort associated with the changing of the dressing material, and the accumulation of body fluid for wounds with high exudate. However, there is a shift from conventional wound dressing materials to polymeric nanofibers due to their high surface area to volume ratio, high porosity, good pore size distribution, which allows for cell adhesion and proliferation. There is an urgent need to synthesis a biodegradable composite that is resistant to bacterial infection. In this study, an electrospun polylactide (PLA) composite suitable for wound dressing, with enhanced antimicrobial and mechanical properties, was produced. The neat PLA, PLA/CH (10 wt.%), PLA/CH (5 wt.%), PLA/CHS (10 wt.%), PLA/CHS (5 wt.%), PLA/CH (2.5 wt.%) /CHS (2.5 wt.%) and PLA/CH (5 wt.%)/CHS (5 wt.%), were electrospun using 0.14 g/ml solution. Results show that crystallinity (67.6%) of neat PLA declined by 3.8% on the addition of 2.5 wt.% chitin/chitosan with improved hydrophilicity of the composite. The tensile strength of neat PLA (0.3 MPa) increased (0.6 MPa) with 2.5 wt.% chitin/chitosan addition. The slight increase in the glass transition temperature from 75°C for neat PLA to 78°C of the composite fibre, showed improved ductility. The fibres showed little beads, hence suitable for wound dressing. The electrospun mats have good water absorption capacity and strong resistance against *Staphylococcus aureus*. Good performance was attained at 5 wt.% of chitin, chitosan and hybrid reinforcements. Therefore, a PLA/chitin/chitosan composite is recommended as a wound dressing material.

Keywords:

chitin, chitosan, hydrophilicity, polylactide acid, skin, wound, staphylococcus-Auerus

1. INTRODUCTION

Wound healing is a global medical concern, and has thrown up other challenges, including the increasing incidence of obesity, type II diabetes, and ageing populations [1]. In 2018, retrospective analysis of Medicare beneficiaries identified that ~8.2 million people had wounds with or without infections. The Medicare cost estimate for acute and chronic wound treatment ranges from $28.1 billion to $96.8 billion. The highest expenses were for surgical wounds followed by diabetic foot ulcers [2]. In the US alone, over 100,000 surgeries performed daily involve surgical wounds. The anticipated market shares for wound care products are expected to reach ~US$25000 million. The use of growth factors to accelerate the healing of wounds offers a tremendous promise as a therapeutic approach in treating chronic wounds. Clinicians are unable to recommend the use of advanced dressings, however, because of their high cost, although these are more conducive to healing, require fewer dressing changes, and less care [3].

In terms of effectiveness, a wound dressing material should be able to keep the wound moist, stop bleeding, improve oxygen

absorption, remove exudates, be biodegradable, prevent bacterial infection and enhance the healing process [4–6]. The authors, [7] explicitly corroborated that wound dressings currently available in the Western Nigerian market do not fully address all the physiological issues associated with chronic wounds. The study primarily focused on bacterial clearance, leaving other factors inhibiting wound bed re-epithelization and wound closure unattended. It should be noted that a wound dressing material should be able to mimic the skin extracellular matrix (ECM). In this regard, nano fibres that are similar to ECM protein and pore size are important factors that facilitate cell respiration, haemostasis, exudate removal and moisture retention [8]. Electrospinning is considered one of the best methods of producing 3D nano-fibrous materials for the dressing of chronic wounds. Most electrospun fibres possess the desirable properties of an ideal wound treatment material. Although electrospinning is a simple and quick method in the fabrication of nano-fibrous scaffolds, there still exist challenges in the fabrication of scaffolds with complex structures, such as the homogeneous distribution of pores, thus limiting its application in biomedicine. In the study, [9] observed that the addition of particles can lead to the formation of a porous fibre network, which enables the material to absorb water and solvents. The introduction of new biopolymers and fabrication techniques that offer advantageous characteristics in wound dressing materials is important [8].

Polylactic acid (PLA) is obtained from natural raw materials such as maize and its degradation products including H_2O and CO_2. Their intermediate products, being hydroxyl and lactic acid, can be absorbed by the body [10, 11]. However, PLA has drawbacks like poor ductility and to improve on this property, it has been reinforced in recent times with different materials to form various composites. For example, [12] prepared a nano-fibre membrane of polylactic acid/polybutylene, carbonate/graphene oxide by electrospinning and noticed that the incorporation of graphene oxide (GO) leads to the improvement in the hydrophilicity of the PLA/PBC/GO membrane. This was attributed to the presence of the oxygen rich functional group in graphene oxide (GO), which reduces the highly hydrophobic ester group in PLA/PBC. Furthermore, [13] fabricated a novel high performance ductile polylactic acid nano scaffold coated with poly(vinyl alcohol) (PVA). The results showed that the nano-fibre demonstrated good hydrophilicity and mechanical properties. The study suggested that the improvement in the tensile strength was due to the increase in the tear resistance of the branch PVA fibres compared to the linear membrane rather than the presence of a physical/chemical bond between the polymers. Chitin (CH) and its derivative chitosan (CHS) are obtained from marine exoskeletons. Chitosan is known for its antibacterial, tumoricidal, natural blood clothing, wound healing and scar elimination properties [4]. Unfortunately, it is extremely difficult to electrospin chitosan, because of its high viscosity and polyelectrolyte nature [14] and specific intra and inter molecular interactions [15], which causes poor entanglement of the chains. Thus, chitosan is often blended with natural and synthetic polymers. From literature, there is little or no work on PLA/chitin/chitosan composite. PLA and chitin are known to be hydrophobic, while chitosan on the other hand is hydrophilic due to the amino group, therefore blending these biopolymers will enhance the hydrophilic behaviour of the composite. Thus, this work evaluates neat PLA, PLA/chitin, PLA/chitosan and PLA/chitin/chitosan fibre composites, to evaluate its physiochemical properties and ascertains their potential use in the management of surgical wounds around the abdominal region.

2. MATERIALS AND METHOD

2.1. Materials

Polylactic acid (average molecular weight 250,000 g/mol), dichloromethane 95% purity (England). Water used in all the tests was Milli-Q water (Millipore, USA). Bacterial strains of Methicillin-resistant *Staphylococcus aureus* obtained from South Africa was utilized in this study.

2.2. Method

14 g of PLA was dissolved in 100 ml of dichloromethane to produce solution of 0.14 g/ml viscosity. Then, 5 and 10 wt.% chitin and chitosan respectively were added to the solution and stirred continuously until homogenous mixture was achieved. This was followed by electrospinning at a constant voltage of 26 kV, with 90°C spinneret inclination at room temperature (28°C). A stationary Aluminum plate kept at 121 mm from the tip of the spinneret was used as the collector.

2.3. Characterization of electrospun fibre mat

2.3.1. X-ray diffraction (XRD)

The X-ray diffractometry measurements were performed using an EMPYERN diffractometer model XRD-600 at the National Geosciences Research Laboratory, Kaduna. The facility uses CuKα radiation (λ = 1.540598 Å, Ni-filter) at 40 kv, 30 mA. Without any preferred orientation, the samples were scanned in steps of 0.026261° in the 2θ in the range of 4.99–75.00° using a count time of 29.7 s per step.

The crystallinity index (*Crl*) for the neat PLA and the composites mats were calculated using Equation (1) [16].

$$Crl(\%) = \left(\frac{Ic}{Ic + Ia} \right) \times 100 \tag{1}$$

where *Ic* and *Ia* represent the intensities of the crystalline and the amorphous regions respectively.

2.3.2. Thermogravimetric analysis (TGA)

Analysis of samples was carried out on TGA Q500 instrument where 2 mg of samples were heated to 750°C at 10°C/min. The temperature for the onset of thermal decomposition (T_{onset}), temperature at the end of decomposition (T_{finish}) and the temperature at which decomposition was maximum (T_{max}) were deduced from the thermograms.

2.3.3. Scanning electron microscopy (SEM)

The micrographs of samples were produced via a scanning electron microscopy model Phenom Eindhoven, Netherlands situated at Amadu Bello University, Zaria. It works with an electron intensity beam of 15 kV, while the samples were mounted on a conductive carbon imprint left by the adhesive tape. This is usually prepared by placing the samples on the circular holder and coated for 5 min to enable it conduct electricity. Free online software, Image J was used to determine the pore size and fibre diameter of electrospun mats.

2.3.4. Differential scanning calorimetry (DSC)

Thermal characteristics of 7–8 mg of the electrospun samples were determined using a differential scanning calorimetry (DSC) device (Mettler Toledo Equipment DSC1 star system) operated from 25 to 250°C at 10°C/min. High pressure pans were used for the test and heat flow was measured as a function of the temperature and time.

2.3.5 Tensile test

Tensile strength characteristics of the neat PLA and the composites mats were determined using an Instron 3369M tensometer located at the Centre for Energy Research and Development, Obafemi Awolowo University, Ile-Ife Nigeria. Each sample was fixed and held firmly at both ends by the gauge as the load was applied until the sample finally failed.

2.3.6. Water absorption test

Water absorption of the fibre mat was studied at room temperature. Electrospun fibres were weighed and immersed in 50 ml of water for one month. During this period, the sample was removed from the water, cleaned and reweighed every one week. At the end of the one-month interval, the water absorption was calculated using Equation (2) [17].

$$Water\ uptake\ (\%) = 100 \times \frac{W_{wet} - W_o}{W_o} \tag{2}$$

where:

W_{wet} – is weight of wet fibre;
W_o – initial weight of the sample prior to immersion.

2.3.7. Antibacterial assay

An antibacterial susceptibility test was conducted using several pieces of equipment and tools including an autoclave model YX-280A, a Gallenkamp incubator model from England, a weighing balance manufactured by Ohaus, micropipette, nutrient agar and peptone water (Lab M, UK), petri dishes, cotton wool, antibiotic, *Staphylococcus aureus strain* (ATCC 29213), forceps and a Bunsen burner. The antibacterial assay of the composites was performed on *Staphylococcus aureus* strain (ATCC 29213), which was maintained in glycerol-nutrient broth at 4°C in the Department of Microbiology, University of Lagos, Nigeria. According to a modified protocol by [18], the bacterial strain was sub-cultured in peptone water (Lab M, UK) and incubated at 37°C for 24 h. The culture was serially diluted, and aliquot of appropriate dilution was inoculated into fresh sterile peptone water in McCartney bottles corresponding to the test samples. The composites were incorporated into the inoculated medium with the aid of a sterile pair of forceps. The samples were further incubated at 37°C for 24 h. To determine the total viable counts (TVCs), five folds' serial dilutions of the test samples and controls were made. Aliquot of appropriate dilutions of the test samples and controls were plated onto nutrient agar plates (Lab M, UK) in duplicates using the pour plate technique [19]. The inoculated plates were then incubated at 37°C for 24 h. After 24 h incubation, the developed colonies were counted in duplicates, and the mean values were multiplied by the dilution factor to give TVC. The bacterial colony forming units (CFUs) were compared with the bacteria growth in the absence of the composites (organism control).

3. RESULTS AND DISCUSSION

3.1. Effect of reinforcement on crystallinity of PLA composite fibres

Neat PLA (see Fig. 1) was used as a reference to the entire composite fibre mats. A weak and broad scattering reflection, with low absorption intensity attributed to several degrees of molecules deformation [20] was detected around 2θ = 16.7° and 19.5° for the neat PLA. This is within the range reported by [21] for semi crystalline polymer. Crystalline peaks for chitin and chitosan occurred around 2θ range of 16.5° and 22.5°. This was also observed by [15]. This may be attributed to the intercalation of chitin and chitosan structure within the PLA matrix. However, there was no change in the crystalline peak position for the composite mats at various percentages of reinforcement, when compared with neat PLA. This shows good miscibility and interactions between the composite constituents. This interaction might have occurred due to the hydrogen bonding between the PLA and hydroxyl/amine group of chitin (CH) and chitosan (CHS). A narrow hump was noticed at 2θ range of 33° for the fibre mats with PLA/CH (10 wt.%) and PLA/CH (2.5 wt.%) /CHS (2.5 wt.%). The crystallinity index of the fibre mats is shown in Table 1. The high degree of crystallinity of the electrospun neat PLA and PLA/CHS (5 wt.%) fibres when compared to the other composites was ascribed to the higher stretching of the polymer chains leading to a higher degree of molecular organization [22]. Adding a hybrid of chitin and chitosan at varying weight percentages lowers the degree of crystallinity of PLA by 3.8%. [23] observed that the crystallinity of PLA decreased by 2 and 8% when it was reinforced with 10 and 35 wt.% of Titanium oxide respectively. The lower degree of crystallinity improves degradability, and solves the hydrophobic problem of PLA, which is a key factor in improving drug release and drug loading efficiency [24, 23] thus, making the fibre mats useful for wound dressing.

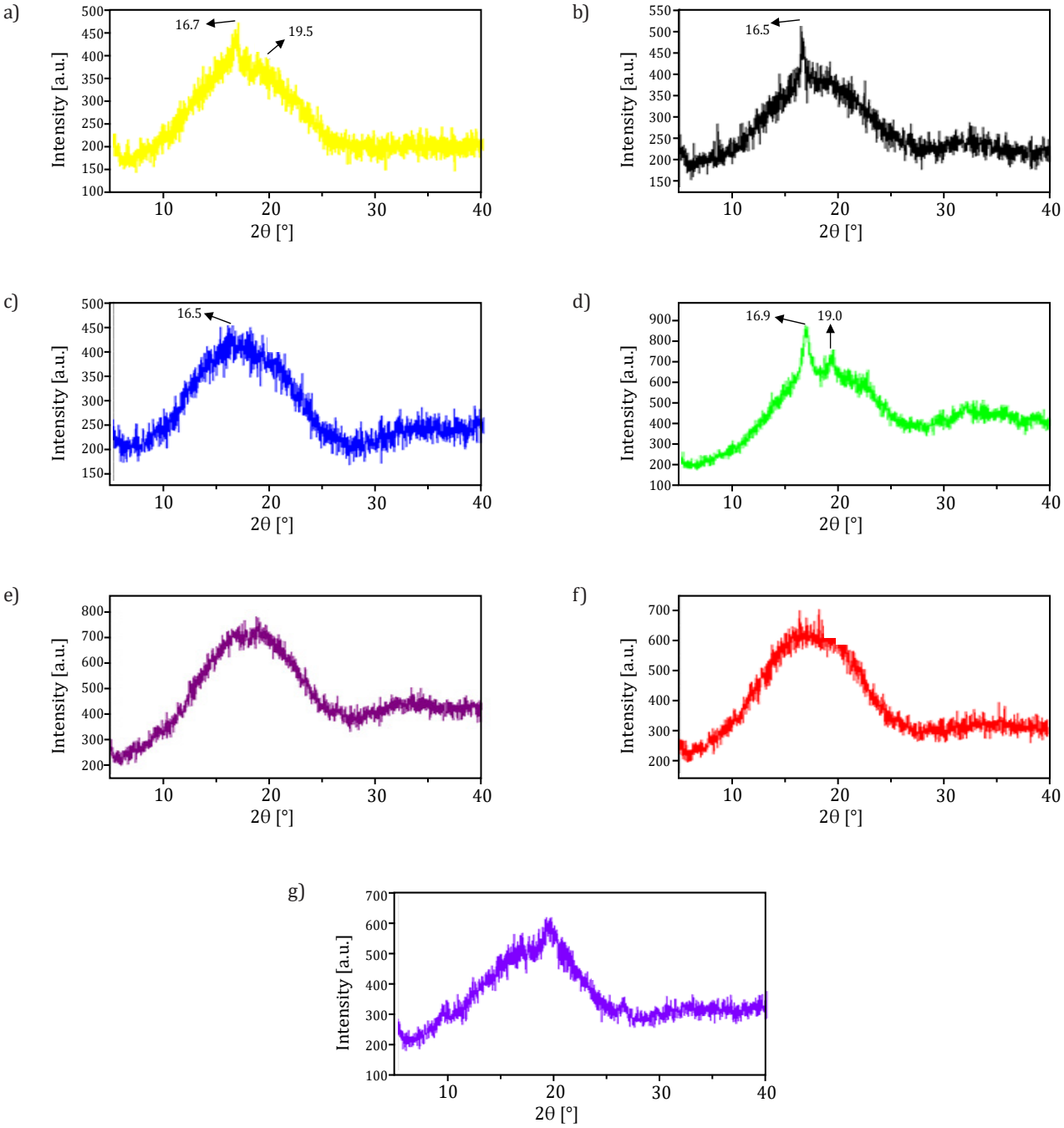

Fig. 1. XRD of electronspun PLA and composite fibre: a) neat PLA; b) PLA/CH (5 wt.%); c) PLA/CHS (5 wt.%); d) PLA/CH (2.5 wt.%)/CHS (2.5 wt.%); e) PLA/CH (10 wt.%); f) PLA/CHS (10 wt.%); g) PLA/CH (5 wt.%)/CHS (5 wt.%)

Table 1
Crystallinity of the electrospun fibre

Electrospun fibre	Crystallinity [%]
PLA	67.6
PLA/CH (10 wt.%)	65.1
PLA/CH (5 wt.%)	67.1
PLA/CHS (10 wt.%)	66.7
PLA/CHS (5 wt.%)	67.6
PLA/CH (2.5 wt.%) /CHS (2.5 wt.%)	65.3
PLA/CH (5 wt.%)/CHS (5 wt.%)	65.8

3.2. Thermal degradation response of the reinforced PLA composite

The TGA thermogram (see Fig. 2) of neat PLA showed a range of thermal degradations between 311–364^{0}C with initial mass loss of 25% and 43%. This degradation temperature for neat PLA falls within the range reported by earlier researchers [25, 26]. The residue decomposes finally at 542°C. The fibre mat composites showed, thermal degradation of 301–379°C, 272–348°C, 257–339°C, 287–416°C, 287–405°C and 292–377°C, for PLA/CHS (10 wt.%), PLA/CH (2.5 wt.%)/CHS (2.5 wt.%), PLA/CHS (5 wt.%), PLA/CH (5 wt.%), PLA/CH (5 wt.%)/CHS (5 wt.%), PLA/CH (10 wt.%) respectively. The degradation temperature of chitin has been found to occur around 400°C. [27–29] reported that chitosan exhibited two stages of degradation, with the loss of water molecules in the first stage. However, this result does not agree with what was observed in the present study, where three stages of decomposition were observed. The first stage, which is the loss of water molecules due to hydrophilic nature of chitin and chitosan, was not visible in these spectra, since their percentage in the matrix was relatively small and it also confirms that there was complete vaporization of Dichloromethane after electrospinning. The second stage is at 342–369°C, with the decomposition of the pyranose ring along the polymer backbone to form a complex adduct. The third stage was at 417–415°C, and is the decomposition of the obtained adducts. This is consistent with the works of [15, 30] where it was reported that the thermal stability of electrospun chitosan reinforced with chitin nanocrystals is 180°C. A similar thermal stability of ~185°C was obtained in this present study. The studies suggest that all the fibres have the required thermal stability to be used in wound dressing, which will be in-contact with the body.

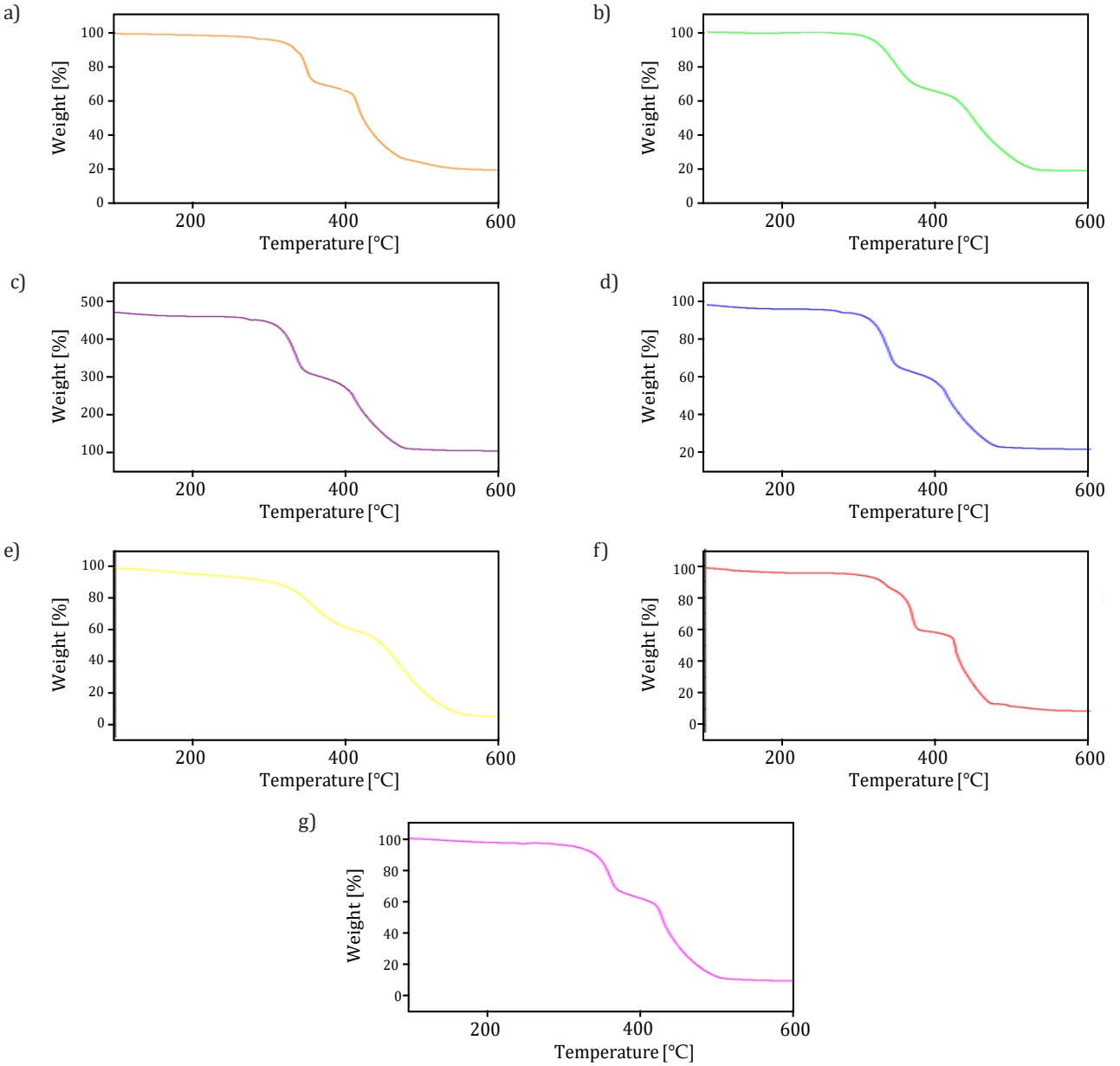

Fig. 2. TGA of electrospun PLA and the fibre mat: a) neat PLA; b) PLA/CH (5 wt.%); c) PLA/CHS (5 wt.%); d) PLA/CH (2.5 wt.%)/CHS (2.5 wt.%); e) PLA/CH (5 wt.%)/CHS (5 wt.%); f) PLA/CHS (10 wt.%); g) PLA/CH (10 wt.%)

From the TGA curve (see Fig. 2), it was observed that, the neat PLA fibre is more thermally stable than the fibre mats of PLA/CHS (10 wt.%), PLA/CH (2.5 wt.%) /CHS (2.5 wt.%), PLA/CHS (5 wt.%), PLA/CH (5 wt.%). This is consistent with the works of [31, 32]. According to the authors [15] who reinforced PLA with PVA, they observed that the decomposition temperature of the composite was reduced in comparison with the neat PLA. This result also showed that the compatibility and interfacial bonding decreases by mixing of both PLA polymer and fibre [32]. The presence of the fibre in PLA destabilized the PLA matrix, where some portion of the polymer is replaced with less thermally stable fibres in the composite materials [31]. In the study, [33] attributed this to the thermal instability of PLA. The reduction in thermal stability does not alter the properties of the scaffold when used at biological temperatures (37°C) [34] and is therefore deemed insignificant in practical terms [35]. Conversely, PLA/CH (5 wt.%) and PLA/CH (5 wt.%) /CHS (5 wt.%) were more stable when compared with the neat PLA; this may be attributed to pronounced particle interaction within the fibre matrix. Similar results were also obtained by [36, 37].

3.3. Decomposition characteristics of PLA fibre composites

The DTG thermogram (see Fig. 3) showed maximum decomposition temperature at 399°C, 483°C, 385°C. 411°C, 378°C, 403°C, 409°C for Neat PLA, PLA/CH (5 wt.%)/CHS (5 wt.%), PLA/CHS (5 wt.%), PLA/CH (10 wt.%), PLA/CH (2.5 wt.%)/CHS (2.5 wt.%), PLA/CH (5 wt.%) and PLA/CHS (10 wt.%), respectively. Thus, some of the composites (478°C, 428°C, and 423°C) showed strong resistance to heat before decomposing and could therefore serve as a hot packaging material [38].

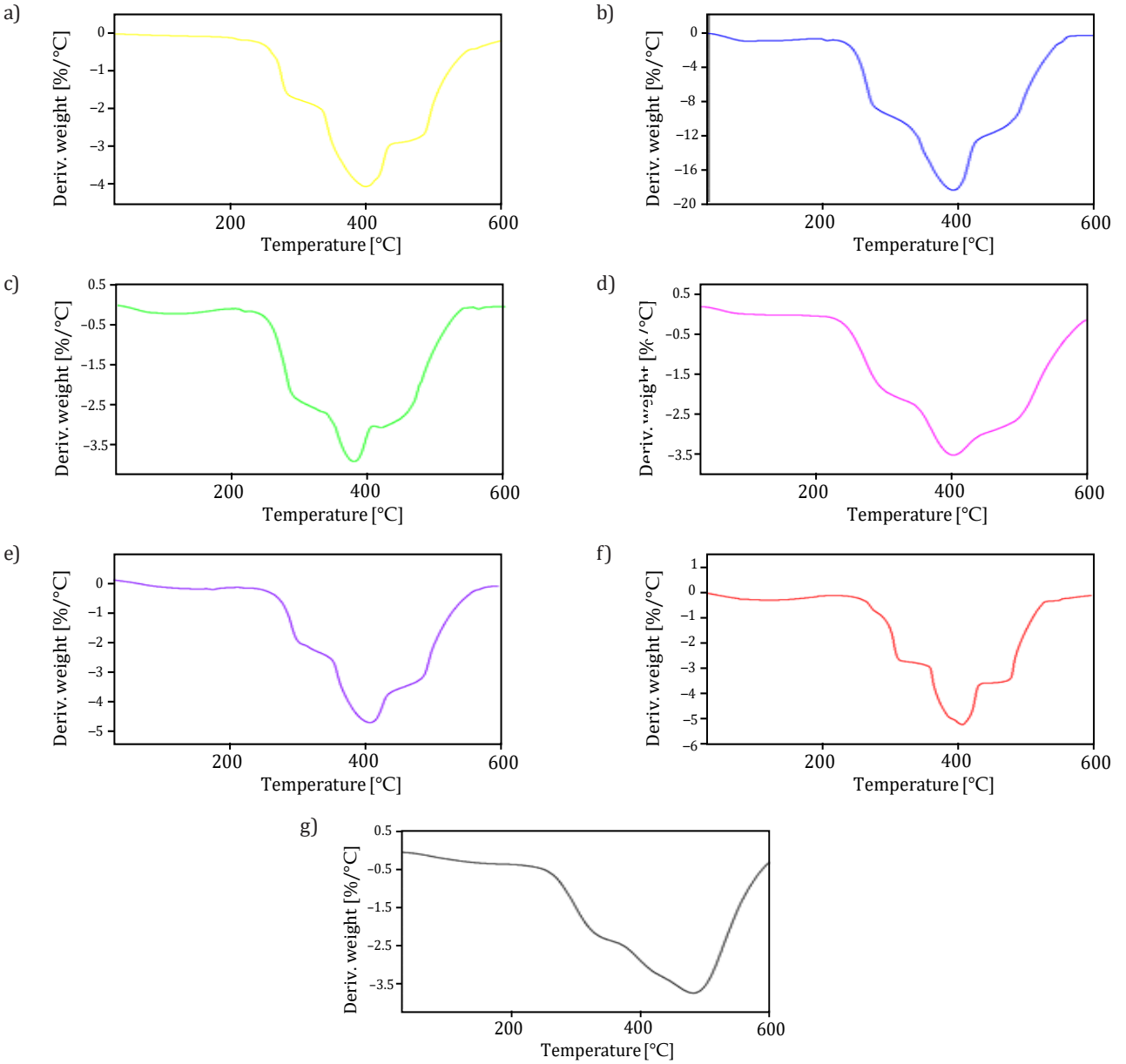

Fig. 3. DTG of electrospun PLA and the composite fibre mat: a) neat PLA; b) PLA/CHS (5 wt.%); c) PLA/CH (2.5 wt.%)/CHS (2.5 wt.%); d) PLA/CH (5 wt.%); e) PLA/CH (10 wt.%); f) PLA/CHS (10 wt.%); g) PLA/CH (5 wt.%)/CHS (5 wt.%)

3.4. Glass transition temperature (T_g) analysis of electrospun PLA and composite fibre

Figure 4 shows the DSC thermogram of electro spun PLA and PLA composites with varying percentages of reinforcement.

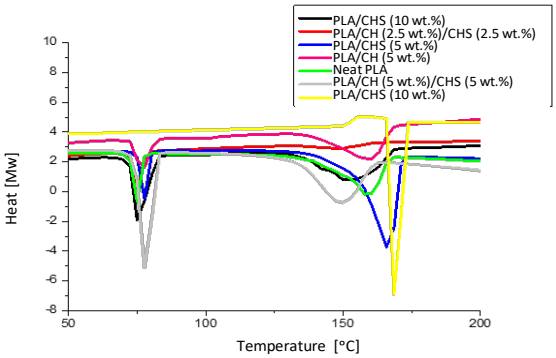

Fig. 4. DSC curve of neat PLA and composite fibre

The T_g of the neat PLA, PLA/CHS (10 wt.%), PLA/CH (2.5 wt.%)/CHS (2.5 wt.%) are the same (75°C), while that of PLA/CHS (5 wt.%),PLA/CH (5 wt.%) have a T_g of (77°C) and PLA/CH (5 wt.%)/CHS (5 wt.%) a T_g of (78°C), which are higher than that of neat PLA. PLA/CH (10 wt.%), did not show any glass transition temperature. A slight increase in the glass transition temperature of the composite shows an increase in the ductility of the reinforced fibre mat material. Thus, PLA/CHS (5 wt.%),PLA/CH (5 wt.%), PLA/CH (5 wt.%)/CHS (5 wt.%) is a suitable material for wound dressing, due to its enhanced ductility. This result is in agreement with [31] who reported a slight increase in T_g of PLA reinforced with 10 wt.% of kenaf fibre. However, T_g reported here is a little higher than the one observed in the literature [12, 23, 31]. The increase in the glass transition temperature is due to the restriction of polymer chain mobility within the interface caused by the hydrogen bonding created between the PLA fibre surface and the fibre reinforcement [39, 40]. The formation of a single glass transition temperature confirms that the composite blend is miscible. A cold crystalline peak was noticed at 155°C. For PLA/CH (10 wt.%), which was not observed in the other composites. The presence of cold crystallization has been attributed to freezing of crystallization before the completion of solvent removal from the spun fibre mat [40]. This composite possesses the lowest crystallinity (65.1%) as shown in Table 1. This was also observed in the work of [9] where the low crystallinity was attributed to the presence of cold crystallization. The melting peak for PLA/CH (5 wt.%) and neat PLA is the same (159°C); PLA/CHS (10 wt.%) and PLA/CH (2.5 wt.%)/CHS (2.5 wt.%) have their melting peak at 152°C while that of PLA/CHS (5 wt.%), PLA/CH (10 wt.%) and PLA/CHS (wt.%)/CH (5 wt.%) occurred at 165°C, 169°C and 149°C respectively. It was observed that the melting peak of PLA/CHS (10 wt.%), PLA/CH (2.5 wt.%)/CHS (2.5 wt.%) and PLA/CHS (5 wt.%)/CH (5 wt.%) is lower than that of neat PLA while PLA/CHS (5 wt.%), PLA/CH (10 wt.%) has a higher melting peak. The increase in this melting temperature might be due to the rearrangement of molecular chain in the regular crystals [12].

3.5. Morphology features of electrospun PLA and composite fibre

Figure 5 shows the electrospun fibre morphology while Figure 6 shows average fibre diameter distribution for neat PLA and its composites. The morphology reveals that the fibres were distributed randomly in a non-woven formation. The fibre diameter of the neat PLA was found to be 14.53 nm. PLA/CH (5 wt.%), PLA/CH (2.5 wt.%)/CHS (2.5 wt.%), PLA/CH (10 wt.%) have a fibre diameter of 15.95 nm, 16.85 nm, 15.15 nm respectively. The increase in fibre diameter of PLA, with the addition of reinforcement may be attributed to an increase in solution viscosity in agreement with the observation of [21].

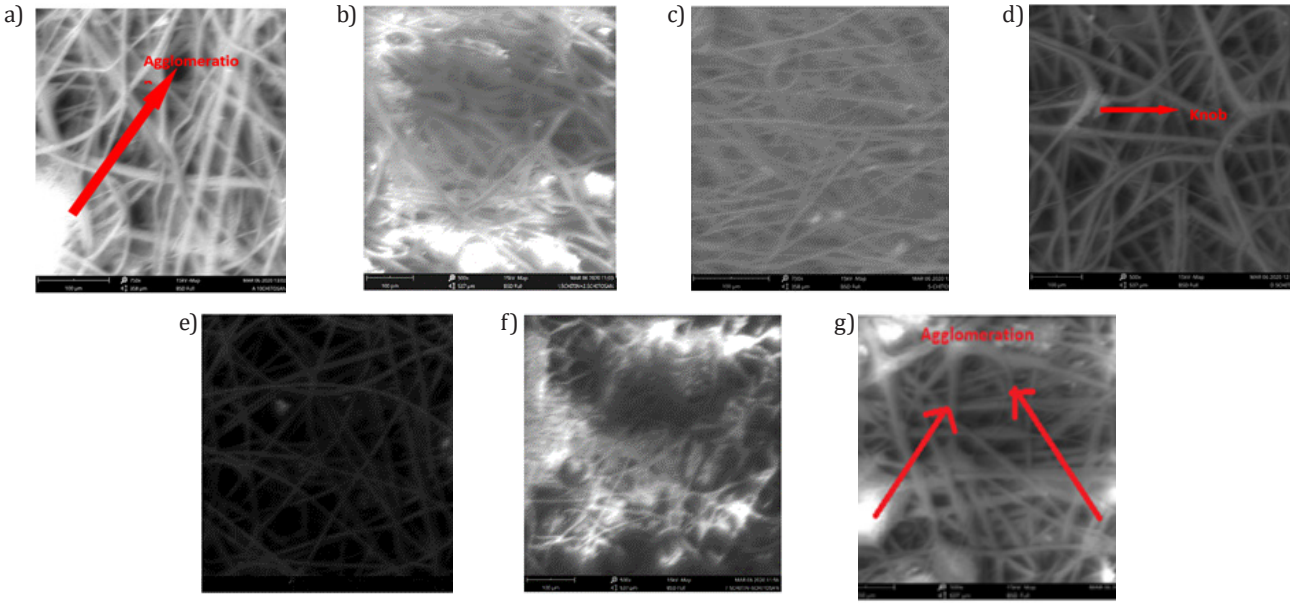

Fig. 5. The SEM morphology of: a) PLA/CHS (10 wt.%; b) PLA/CH (2.5 wt.%)/CHS (2.5 wt.%); c) PLA/CHS (5 wt.%); d) PLA/CH (5 wt.%); e) neat PLA; f) PLA/CH (5 wt.%)/CHS (5 wt.%); g) PLA/CH (10 wt.%)

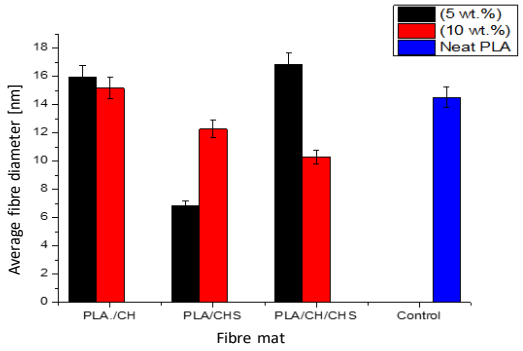

Fig. 6. Fibre diameter of electrospun fibre

Conversely, PLA/ CHS (5 wt.%), PLA/CHS (10 wt.%) and PLA/CH (5 wt.%)/CHS (5 wt.%) showed fibre diameter of 6.86 nm, 12.27 nm, and 10.29 nm respectively, which is lower than that of neat PLA. This could be attributed to the alleviation of the clogging issue arising from agglomeration during electrospinning. The fibres exhibited a relatively uniform fibre diameter. A knob was observed in PLA/CH (5 wt.%), which might be due to the agglomeration of micro-particles that did not completely dissolve in the PLA matrix [41]. The presence of beads was also noticed in PLA/CHS (5 wt.%), PLA/CH (10 wt.%) and PLA/CHS (10 wt.%). Neat PLA has an average pore diameter of 22 m, which is higher than that of the composite's fibres. The pore diameters of the composites were 16 µm, 13 µm, 11 µm, 13 µm, 10 µm and 15 µm for PLA/CHS (10 wt%), PLA/CH (2.5 wt%)/CHS (2.5 wt.%), PLA/CHS (5 wt.%), PLA/CH (5 wt.%), PLA/CH (5 wt.%)/CHS (5 wt.%) and PLA/CH (10 wt.%) respectively. The pore sizes were a result of the irregular deposition of the fibres. However, the pore diameter reported here is higher than the one reported by [24]. In the research of [36] on electrospun polylactic acid and chitosan using different solvents, they noted that a uniform fibre diameter was obtained at 0.4 wt.% chitosan. However, in this present study, a uniform fibre diameter was obtained at various weight fractions for a single solvent.

3.6. Strength characteristics of PLA and its composite

The mechanical strength of a composite nano fibre is quite important for its potential use as a wound dressing material. The tensile strengths of PLA/CH (2.5 wt.%)/CHS (2.5 wt.%) fibre and PLA/CHS (5 wt.%) are 0.60 MPa and 0.40 MPa respectively, which are superior to neat PLA (0.30 MPa), while the rest of the fibre mats have lower tensile strength. From Figure 7, it is observed that there is a minimum percentage of reinforcement for peak tensile strength (0.60 MPa) which corresponds to PLA/CH (2.5 wt.%)/CHS (2.5 wt.%) reinforcement. At 10 wt.% fraction of chitin filler, the tensile strength decreased to 0.1MPa. However, chitosan reinforcement seems to have better properties compared to chitin. A similar report was observed by [35] who electrospun a PLA scaffold coated with PVC (poly vinyl alcohol) and observed that the tensile strength of reinforced fibre mat was better than the neat PLA. The study attributed this to an increase in the tear resistance of the branched PVA fibres (i.e., web-like fibres, parallel PLA fibres bounded to each other by PVA fibres of different diameter) and fibre junctions. This report agrees with the findings of [32] where wood fibre was used to reinforce PLA. It was also noted that the tensile strength of the composite was reduced with the increase in the weight fraction of the wood fibre. Again, [17] electrospun a PLA nano-composite fibre mat with hybrid graphene oxide and nano-hydroxyapatite reinforcement and obtained a maximum tensile strength of 0.57 MPa. However, the current study showed a 5% improvement in the tensile property of PLA (0.31 MPa) fibre mat composite.

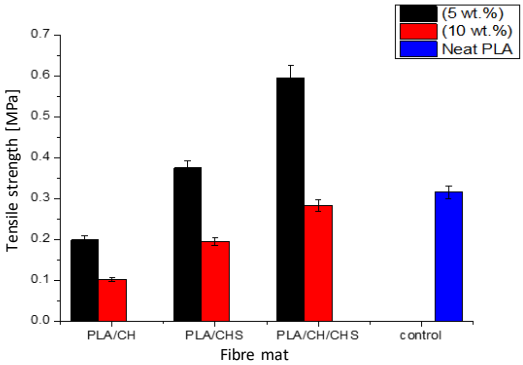

Fig. 7. Tensile strength of the electrospun fibre

3.7. Tensile energy at break

Materials used for internal body fixation should withstand long term loading, making it necessary to study the fibre tensile energy at break (TEB). The convectional testing method for toughness cannot be used as it is not a bulk material. Thus, tensile energy at break (TEB) is used as an alternative [9]. Figure 8 shows the tensile energy at break of the fibre mat. Fibre composite PLA/CH (5 wt.%)/CHS (5 wt.%), PLA/CHS (5 wt.%) and PLA/CH (2.5 wt.%)/CHS (2.5 wt.%) proved to have a superior TEB compared with the neat PLA (0.036 J).

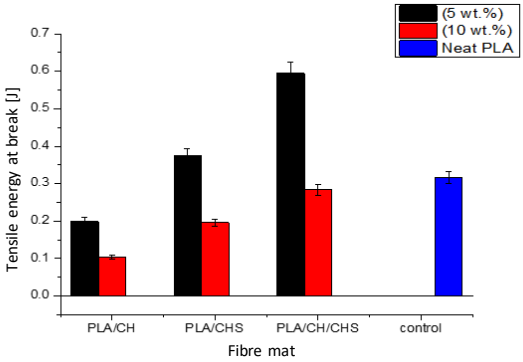

Fig. 8. Tensile energy at break

Fibre mat PLA/CH (5 wt.%)/CHS (5 wt.%) has the highest TEB (0.111 J). Tensile energy at break is a measure of material toughness. Wound dressing materials should be able to withstand long-term loading before failure, especially during the wound swelling phase. Thus, fibre mat PLA/CH (5 wt.%)/CHS (5 wt.%) with the highest TEB is recommended for large surface wounds that tend to swell more during the swelling phase without compromising the property of the material. It

was observed that the TEB is dependent on the weight percentage of the filler. Thus, 5 wt.% reinforcement shows a better TEB and good tensile strength as described above.

3.8. Strain at maximum stress

The fibre mats in Figure 9 did not show any definite pattern in relation to the weight fraction of the filler used. However, PLA/CH (5 wt.%)/CHS (5 wt.%), PLA/CHS (5 wt.%), PLA/CHS (10 wt.%) and PLA/CH (2.5 wt.%)/CHS (2.5 wt.%), showed a better strain before the material yielded. Fibre mat with PLA/CH (5 wt.%)/CHS (5 wt.%), showed the maximum strain (0.18%), which is about a 199% improvement over the neat PLA fibre mat. Thus, this material is recommended for use when the affected part undergoes continuous movement and may exert strain on the material.

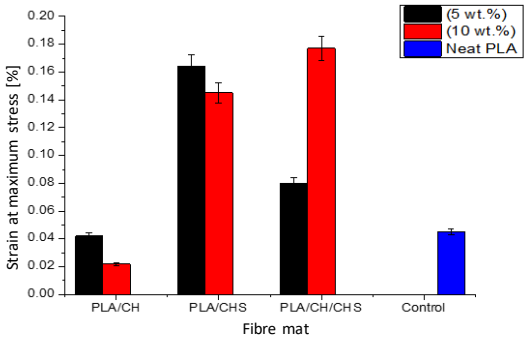

Fig. 9. Strain at maximum stress

3.9. Water absorption capacity of PLA composite

Figure 10 shows the rate of water absorption of the electrospun samples at room temperature.

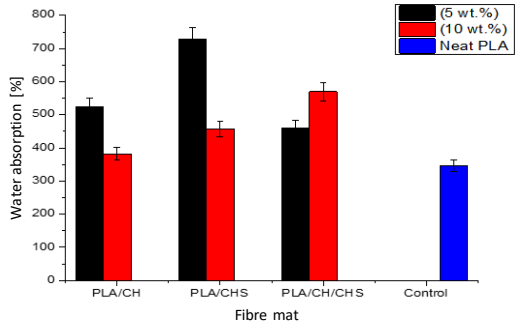

Fig. 10. Water absorption capacity of PLA and its composite

Optimum water absorption capacity was obtained at 5 wt.% chitosan in PLA. The rate of water absorption was observed to be dependent on the percentage weight of the filler. However, as filler content increases, the water absorption capacity decreases. This suggests that the composite pore spaces were more compacted as filler weight increases. Chitosan filler showed better water absorption capacity when compared to chitin in the PLA composite matrix. This improvement by chitosan may be attributed to the formation of an amino group (-NH_2) of the chitosan during deacetylation. Generally, the water absorption capacity of the composites was better than the neat PLA. It is shown by the work of [9], who earlier reported an improvement in water absorption capacity over neat PLA by reinforcing PLA with Bagasse. More importantly, the result reported here showed highest water absorption of ~750%, which is superior to that reported by [17] in a study of electrospun polylactic acid nano-composite fibre mats with hybrid graphene oxide and nano-hydroxyapatite reinforcements (~210%).

3.10. Antimicrobial test

Figure 11 shows the total viable counts (TVCs) of the bacteria exposed to composites, and unexposed bacteria. All the composites show an antibacterial effect against *staphylococcus aureus*.

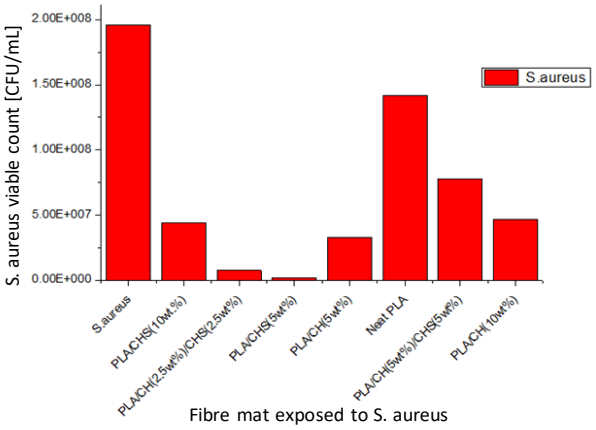

Fig. 11. The total viable counts (TVCs) bacteria exposed to composites and unexposed bacteria

The fibre mat with the composition PLA/CHS (5 wt.%) shows the highest antibacterial effect against *staphylococcus aureus*, with the highest number of reduction in the bacterial population ($1.942 \cdot 10^8$ CFU/ml). The results from this present study agrees with earlier works by [18] who fabricated a chitosan-cellulose composite for wound dressing, and reported that chitosan can effectively kill gram positive *staphylococcus aureus*. At 5 wt.% reinforcement good performance against *staphylococcus aureus* was recorded. Surprisingly, the neat PLA to an extent showed some activity against this bacterium, suggesting that unreinforced PLA has some measures of inherent antimicrobial property. The percentage reduction in the microbial population is 96.0, 99.0, 85.0, 27.0, 60.0 and 70.0% for PLA/CH (2.5 wt.%)/CHS (2.5 wt.%), PLA/CHS (5 wt.%), PLA/CH (5 wt.%), Neat PLA, PLA/CH (5 wt.%)/CHS (5 wt.%), PLA/CH (10 wt.%) respectively. Bacteriostatic and bactericidal are known to be very important in wound healing applications in preventing infection. The authors [42, 43] showed that electrospun nanofibers combining the biocompatibility potential of PVA with 0.01% w/w keratin and the antibacterial property of mupirocin was effective in treating drug resistant wounds. Hence, the PLA/CHS developed

scaffold can be used as a backbone for the development of antibacterial composites containing antibacterial agents that will enhance its antibacterial and bacteriostatic activity. This property was exhibited by chitin and chitosan reinforced PLA composites fibres, making them suitable as wound dressing materials to prevent wound colonization or severe infection. Figure 12 showed the population of staphylococcus bacteria exposed to composites, and unexposed bacteria. The bacteria were exposed to the composites for 24 hours. Physical examination showed sizable number of reductions in the population growth proving that the composites were resistant against staphylococcus aureus development and growth.

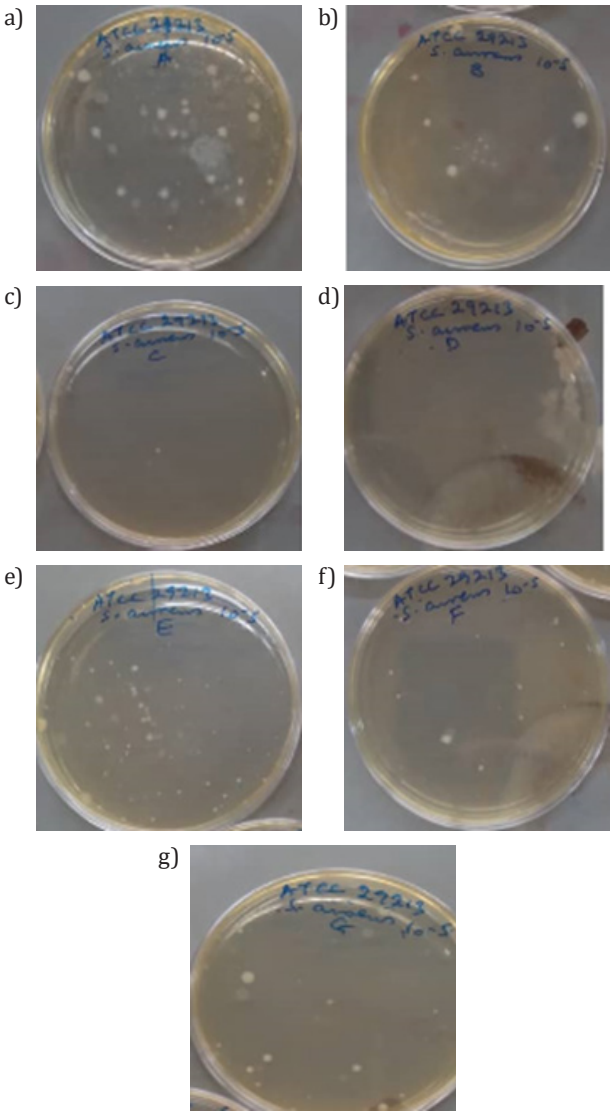

Fig. 12. Reduction in the microbial population of exposed and unexposed bacterial: a) PLA/CHS (10 wt.%); b) PLA/CH (2.5 wt.%)/CHS (2.5 wt.%); c) PLA/CHS (5 wt.%); d) PLA/CH (5 wt.%); e) neat PLA; f) PLA/CH (5 wt.%)/CHS (5 wt.%); g) PLA/CH (10 wt.%)

4. CONCLUSION

An electrospun fibre (PLA/CH/CHS) mat with good morphology suitable for surgical wound dressing was developed using 0.14 g/mL of PLA and fillers in a DCM solvent. The tensile strength of neat PLA (0.3MPa) was improved by 100%. The tensile strain of neat PLA (0.045%) was enhanced (199%) when reinforced with CHS (10 wt.%). The fibre mat has the requisite thermal stability required for wound dressing, (~185°C). The crystallinity of PLA (67.6%) declines by 3.8%, with PLA/CH (10 wt.%) with improvement in hydrophilicity of PLA as increase in water absorption capacity of the fibre mat occurred. Thus, the fibre mat produced is capable of absorbing exudate. The composite showed antibacterial resistance against *staphylococcus aureus* (99.0% efficiency) exhibited by PLA/CH (2.5 wt.%)/CHS (2.5 wt.%) fibre. This fibre mat is suitable for wound dressing to prevent wound infections and as useful backbone for the development of bioactive wound dressings.

REFERENCES

[1] Boateng J.S., Matthews K.H., Stevens H.N.E. & Eccleston G.M. (2008). Wound healing dressings and drug delivery systems: a review. *Journal of Pharmaceutical Sciences*, 97(8), 2892–2923. Doi: https://doi.org/10.1002/jps.21210.

[2] Chandan K.S. (2019). Human wounds and its Burden: An updated Compendium of Estimates. *Advances in Wound Care*, 8(2), 39–49. Doi: https://doi.org/10.1089/wound.2019.0946.

[3] Willi P. & Chandra P.S. (2004). Chitosan and Alginate Wound Dressings: A Short Review. *Trends Biomaterial Artificial Organs*, 18(1), 18–23.

[4] Ilenghoven D., Chan C.Y., Wsr W.A.K., Mohdyussof S.J. & Ibrahim S. (2017). A Review of Wound Dressing Practices. *Clinical Dermatology Open Access Journal*, 2(6), 000133. Doi: https://doi.org/10.23880/CDOAJ-16000133.

[5] Uzun M. (2018). A review of Wound Management Materials. *Journal of Textile Engineering and Fashion Technology*, 1(4), 53–59. Doi: https://doi.org/10.15406/jteft.2018.04.00121.

[6] Zahedi P., Rezaeian I., Ranaei-Siadat S.-O., Jafari S.-H. & Supaphol P. (2009). A review on wound dressings with an emphasis on electrospun nanofibrous polymeric bondages. *Polymer Advance Technology*, 21, 77–95. Doi: https://doi.org/10.1002/pat.1625.

[7] Rahman G.A., Adigun I.A., Yusuf I.F. & Ofoegbu C.K.P. (2006). Wound dressing where there is a limitation of choice. *Nigerian Journal of Surgical Research*, 8(3–4), 151–154. Doi: https://doi.org/10.4314/njsr.v8i3-4.54882.

[8] Adomavičiūtė E., Pupkevičiūtė S., Juškaitė V., Žilius M., Stanys S., Pavilonis A. & Briedis V. (2017). Formation and Investigation of Electrospun PLA Materials with Propolis Extracts and Silver Nanoparticles for Biomedical Applications. *Journal of Nanomaterials*, 1–11, 8612819. Doi: https://doi.org/10.1155/2017/8612819.

[9] Akpan E.I., Gbenebor O.P., Igogori E.A., Aworinde A.K. Adeosun S.O. & Olaleye S.A. (2019). Electrospun porous bio-fibre base on polylactide/natural fibre particles. *Arab Journal of Basic and Applied Sciences*, 26(1), 225–235. Doi: https://doi.org/10.1080/25765299.2019.1607995.

[10] Hidalago I.A., Sojo F., Arvelo F. & Sabino M.A. (2013). Functional electrospun poly(latic acid) scaffolds for biomedical applications: experimental conditions, degradation and biocompatibility study. *Molecular and cellular Biomechanics*, 10(2), 85–105. Doi: https://doi.org/10.3970/mcb.2013.010.085.

[11] Anderson J.M. & Shive M.S. (1997). Biodegradation and biocompatibility of PLA and PLG microspheres. *Advanced Drug Delivery Reviews*, 28(1), 5–24. Doi: https://doi.org/10.1016/s0169-409x(97)00048-3.

[12] Gu X., Li Y., Cao R., Liu S., Fu C., Feng, S. Yang C., Cheng W. & Wang Y. (2019). Novel electrospun Poly(latic acid)/Polybutylene/Graphene oxide nanofiber membranes for antibacterial applications advances. *AIP Advances*, 9(6), 065306. Doi: https://doi.org/10.1063/1.5100109.

[13] Eltom A., Zhong G. & Muhammad A. (2019). Scaffold Techniques and Designs in Tissue Engineering Functions and Purposes: A Review. *Advances in Materials Science and Engineering*, 3429527. Doi: https://doi.org/10.1155/2019/3429527.

[14] Thamarai S.V., Gobinath R., Thirumurugan K. & Mekala N. (2019). Development of Electrospun Wound Dressing for Hemorrhage Control using Biominerals. *International Journal of Recent Technology and Engineering*, 8(2S3), 880–882. Doi: https://doi.org/10.35940/ijrte.B1165.0782S319.

[15] Naseri N., Algan C., Jacobs V., John M. Oksman K. & Mathew A.P. (2014). Electrospun chitosan-based nanocomposites mats reinforced with chitin nanocrystals for wound dressing. *Carbohydrate Polymers*, 109, 7–15. Doi: https://doi.org/10.1016/j.carbpol.2014.03.031.

[16] Juárez-de la Rosa B.A., Quintana P., Ardisson P.I., Yáñez-Limón J.M., Alvarado-Gil J.J. (2012). Effects of thermal treatments on structure of two black coral species chitinous exoskeleton. *Journal of Material Science*, 47, 990–998. Doi: http://dx.doi.org/10.1007%2Fs10853-011-5878-9.

[17] Liu C., Wong H.M., Yeung K.W.K & Tjong S.C. (2016). Novel Electrospun Polylactic Acid Nanocomposite Fiber Mats with Hybrid Graphene Oxide and Nanohydroxyapatite Reinforcements Having Enhanced Biocompatibility. *Polymers*, 8(8), 287. Doi: https://doi.org/10.3390/polym8080287.

[18] Harkins A.L., Duri S., Kloth L.C. & Tran C.D. (2013). Chitosan-cellulose composite for wound dressing material. Part 2. Antimicrobial activity, blood absorption ability and biocompatibility. *Journal of Biomedical Material Research. Part B*, 102(6), 1199–1206. Doi: https://doi.org/10.1002/jbm.b.33103.

[19] Dubey R.C. & Maheshwari D.K. (2012). *Practical microbiology*. 2nd Edition. S. Chand and Company private ltd, (Ed.), New Delhi.

[20] Boland E.D., Pawlowski K.J., Barnes C.P., Simpson D.G., Wnek G.E. & Bowlin G.L. (2006). Electrospinning of bioresorbable polymers for tissue engineering scaffolds. *American Chemical Society Symposium Series*, 918, 188–204. Doi: http://dx.doi.org/10.1021/bk-2006-0918.ch014.

[21] Dong Y., Marshall J., Haroosh H.J., Mohammadzadehmoghadam S., Liu D., Qi X. & Lau K.-T. (2015). Polylactic acid (PLA)/halloysite nanotube (HNT) composite mats: Influence of HNTcontent and modification. *Composites Part A*: *Applied Science and Manufacturing*, 76, 28–36. Doi: https://doi.org/10.1016/j.compositesa.2015.05.011.

[22] Oliveira J.E., Mattoso L.H.C., Orts W.J. & Medeiros E.S. (2013). Structural and Morphological Characterization of Micro and Nanofibers Produced by Electrospinning and Solution Blow Spinning: A comparative study. *Advances in Materials Science and Engineering*. 409572. Doi: https://doi.org/10.1155/2013/409572.

[23] Marsi T.C.O., Ricci R., Toniato T.V., Vasconcellos L.M.R., Vaz Elias M.V., Silva A.D.R., Furtado A.S.A., Magalhães L.S.S.M., Silva-Filho E.C., Marciano F.R., Zille A., Webster T.J. & Lobo A.O. (2019). Electrospun Nanofibrous Poly (Lactic Acid)/Titanium Dioxide Nanocomposite Membranes for Cutaneous Scar Minimization. *Frontiers in Bioengineering and Biotechnology*. Doi: https://doi.org/10.3389/fbioe.2019.00421.

[24] Lu Y., Chen Y.-C. & Zhang P.-H. (2016). Preparation and characterization of Polylactic Acid (PLA)/Polycaprolactone (PCL) Composite Microfiber Membranes. *Fibres and Textiles in Eastern Europe*. 3(117), 17–25. Doi: https://doi.org/10.5604/12303666.1196607.

[25] Qi G. (2013). *Fabrication and characterization of PLA, PHBV and Chitin Nanowisker Blends, Composites and foams for High structural Applications*. University of Toronto [unpublished Master Thesis].

[26] Kancheva M., Toncheva A., Manolova N. & Rashkov I. (2015). Enhancing the mechanical properties of electrospun polyester mats by heat treatment. *Express Polymer Letters*, 9(1), 49–65. Doi: https://doi.org/10.3144/expresspolymlett.2015.6.

[27] Ahyat N.M., Mohamad F., Ahmad A.S. & Azmi A.A. (2017). Chitin and Chitosan Extraction from Portunus Pelagicus. *Malaysian Journal of Analytical Sciences*, 21(4), 770–777. Doi: https://doi.org/10.17576/mjas-2017-2104-02.

[28] Gbenebor O.P., Adeosun S.O., Lawal G.I., Jun S. & Olaleye S.A. (2017). Acetylation, crystalline and morphological properties of structural polysaccharide from shrimp exoskeleton. *Engineering Science and Technology, an International Journal*, 20(3), 1155–1165. Doi: https://doi.org/10.1016/j.jestch.2017.05.002.

[29] Gonçalves R.P., Ferreira W.H., Gouvêa R.F., & Andrade C.T. (2017). Effect of chitosan on the properties of electropunk fibers from mixed poly(Vinyl Alcohol)/chitosan solution. *Materials Research*, 20(40), 984–993. Doi: https://doi.org/10.1590/1980-5373-MR-2016-0618.

[30] Pawlak A. & Mucha M. (2003). Termogravimetric and FTIR studies of chitosan blends. *Termochimica Acta*. 396(1–2), 153–166. Doi: https://doi.org/10.1016/s0040-6031(02)00523-3.

[31] Tawakkal M.A. (2016). Characterization and antimicrobial activity of poly (lactic acid)/kenaf bio-composites containing a natural agent. Vectorial University Melbourne, Australia [unpublished Doctoral Thesis].

[32] Huda M.S., Drzal L.T., Misra M. & Mohanty A.K. (2006). Wood-fiber-reinforced poly (lactic acid) composites: Evaluation of the physiochemical and morphological properties. *Journal of Applied Polymer Science*, 102(5), 4856–4869. Doi: https://doi.org/10.1002/app.24829.

[33] Abdelaal O.A., & Darwish S. M. (2013). Review of Rapid Prototyping Techniques for Tissue Engineering Scaffolds Fabrication. In: *Öchsner* A., da Silva L.F.M. & Altenbach H., *Characterization and Development of Biosystems and Biomaterials*, Springer-Verlag, Berlin – Heidelberg, 33–54.

[34] Meneghello G., Parker D.J., Ainsworth B.J., Perera S.P., Chaudhuri J.B., Ellis M.J. & De Bank P.A. (2009). Fabrication and characterization of poly(lactic-*co*-glycolic acid)/polyvinyl alcohol blended hollow fibre membrane for tissue engineering applications. *Journal of Membrane Science*, 344(1–2), 55–61. Doi: http://dx.doi.org/10.1016/j.memsci.2009.07.034.

[35] Abdal-hay A., Hussein K.H., Casettari L., Khalil K.A & Hamdy A.S. (2015). Fabrication of novel high performance ductile poly(lactic acid) nanofiber scaffold coated with poly(vinyl alcohol) for tissue engineering application. *Material Science and Engineering: C*, 60, 143–150. Doi: https://doi.org/10.1016/j.msec.2015.11.024.

[36] Thomas M.S., Pillai P.S.K., Faria M., Cordeiro N., Barud H., Thomas S. & Pothen L.A. (2018). Electrospun polylactic acid-chitosan composite. A bio-based alternative for inorganic composites for advance application. *Journal of Material Science: Materials in Medicine*, 29:137. Doi: https://doi.org/10.1007/s10856-018-6146-1.

[37] Silverajah V.S, Ibrahim N.A., Yunus W.Z.W., Hassan H.A. & Woei C.B. (2012). A comparative study on the mechanical, thermal and morphological characterization of poly(lactic acid)/epoxidized palm oil blend. *International Journal of Molecular Sciences*, 13(5), 5878–5898. Doi: https://doi.org/10.3390/ijms13055878.

[38] Murariu M., Dechief A.-L., Ramy-Ratiarison R., Paint Y., Raquez J.-M. & Dubois P. (2015) Recent advances in production of poly (lactic acid) (PLA) nanocomposites: a versatile method to tune crystallization properties of PLA. *Nanocomposites*, 1(2), 71–82. Doi: https://doi.org/10.1179/2055033214Y.0000000008.

[39] Hossain K.M.Z., Felfel R.M., Rudd C.D., Thielemans W. & Ahmed I. (2014). The effect of cellulose nanowhiskers on the flexural properties of self-reinforced polylactic acid composites. *Reactive & Functional Polymer*, 85, 193–200.

[40] Chen H.-C., Tsai C.-H. & Yang M.-C. (2011). Mechanical properties and biocompatibility of electrospun polylactide/poly(vinylidene fluoride) material. *Journal of Polymer Research*, 18(3), 319–327. Doi: https://doi.org/10.1007/s10965-010-9421-5.

[41] Zhao N., Shi S., Lu G. & Wei M. (2007). Polylactide (PLA)/layered double hydroxides composite fibers by electrospinning method. *Journal of Physics and Chemistry of Solids*, 69(5–6), 1564–1568. Doi: https://doi.org/10.1016/j.jpcs.2007.10.046.

[42] Amajuoyi J.N., Ilomuanya M.O., Asantewaa-Osei Y., Azubuike C.P., Adeosun S.O. & Igwilo C.I. (2020). Development of electrospun Keratin/coenzyme Q10/poly vinyl alcohol nano fibrous scaffold containing mupirocin dressing for infected wounds. *Future Journal of Pharmaceutical Sciences*, 6(25). Doi: https://doi.org/10.1186/s43094-020-00043-z.

[43] Ilomuanya M.O., Okafor P.S., Amajuoyi J.N., Onyejekwe J.C., Okubanjo O.O., Adeosun S.O. & Silva B.O. (2020). Polylactic acid-based electrospun fiber and Hyaluronic acid-valsartan hydrogel scaffold for chronic wound healing. *Beni-Suef University Journal of Basic and Applied Sciences*, 9(31). Doi: https://doi.org/10.1186/s43088-020-00057-9.